Montanuniversität Leoben

High temperature mechanical testing of novel Cu-Nb nanocomposites

Master Thesis

Mladen-Mateo Primorac

Department of Materials Physics, Montanuniversität Leoben, Austria

Department of Nuclear Engineering, University of California Berkeley, USA

Leoben, November 2013

“Non est ad astra mollis e terris via.”

Lucius Annaeus Seneca

Eidesstattliche Erklärung

Ich erkläre an Eides statt, dass ich diese Arbeit selbstständig verfasst, andere als die angegebenen Quellen und Hilfsmittel nicht benutzt und mich auch sonst keiner unerlaubten Hilfsmittel bedient habe.

Affidavit

I declare in lieu of oath, that I wrote this thesis and performed the associated research myself, using only literature cited in this volume.

_____ _____

Datum Signature

Index

1 Introduction

The demand for harder, better and more functional materials has stimulated scientists to investigate a new material category – nanocrystalline (nc) and ultrafine grained (ufg) materials [1]. These materials feature a very small structural size on the order of a few nanometres (1 nm = 10^{-9} m) in at least one direction. As reported in many works, this class of materials exhibits extraordinary properties, for example very high strength, good thermal, optical and magnetic properties [2, 3].

One of these promising nanomaterials is studied in this work, namely a two phase system composed of the body centred cubic (bcc) element niobium (Nb) and face centred cubic (fcc) element copper (Cu). Cu and Nb have a positive heat of mixing. A phase diagram of the two immiscible elements is shown in Fig. 1.1 [4], whereas only very limited solubility is shown for Cu as well as Nb at elevated temperatures, which diminishes at room temperature (RT). Furthermore the phase diagram indicates that the elements do not form any intermetallic compounds. In the last years several investigations were carried out in order to determine the properties of this composite. The copper niobium (Cu-Nb) composite exhibits outstanding performances, for example high strength and hardness, a high thermal stability and enhanced conductivity, depending on the amount of Nb in the Cu matrix [5-13].

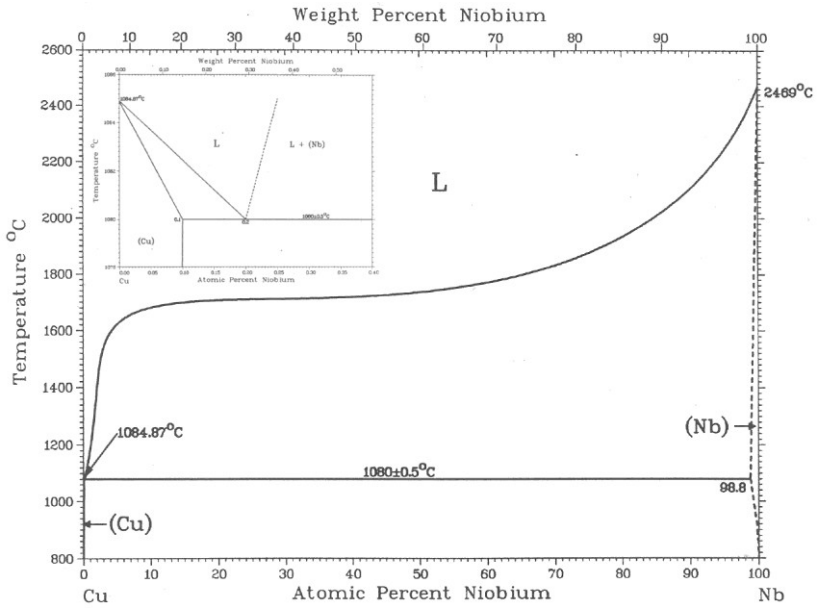

Fig. 1.1: Binary copper niobium phase diagram showing small solubility for both elements and no formation of any intermetallic compounds [4].

One of the application areas for Cu-Nb composites is as ultra high strength conducting materials. According to Botcharova et al. [5-7] nc Cu-Nb alloys exhibit high strength and high con-

ductivity. The insoluble Nb was used in order to strengthen the Cu matrix by particle strengthening. The composite was manufactured by mechanical alloying with a maximum Nb content of 20 at.% [5].

Increasing the amount of Nb in the composite to 50 at.% by a sputtering process for alternating material deposition, a nanolayered structure can be achieved, according by Misra, Mara and co-workers [8-10] as can be seen in Fig. 1.2. The layer thickness of the multilayered structure is tuneable because of the processing route.

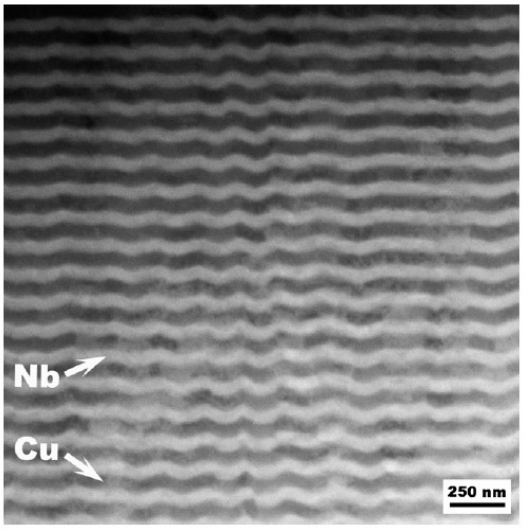

Fig. 1.2: Cu-Nb nanolayered composite with a layer thickness of approximately 70 nm, scanning electron microscope (SEM) backscattered electron image [9].

In the work of Misra and co-workers, for example [11-13], the radiation tolerance after helium (He) ion implantation was investigated. The interface has a special orientation (Kurdjumov-Sachs orientation relationship) [11] between the layers of Cu and Nb and is therefore favourable for absorbing point defects.

It is anticipated that such nanocomposites could be used as material for application in harsh radiation environments such as nuclear reactors due to the enhanced radiation damage tolerance compared to other bulk materials. To maintain the before mentioned properties, the preservation of the nanoscaled microstructure at higher temperatures (operating temperatures of a reactor are approximately 400°C) is indispensable.

The aim of this work is to create a novel Cu-Nb composite for high temperature applications in harsh radiation environments. The interfaces between Cu and Nb of the investigated polycrystalline composite will be general grain boundaries, not only exhibiting the before mentioned Kurdjumov-Sachs relationship as in the two dimensional multilayered composite. The material will be manufactured by a severe plastic deformation (SPD) technique, the high

pressure torsion (HPT) process. Due to the high shear strains that are realized in such a process, a pronounced grain refinement occurs. The microstructure is refined to the submicron range [14]. The manufacturing of the specimens, a microstructural characterisation and microhardness measurements will be realised at the Department of Materials Physics at the Montanuniversität Leoben, Austria.

In order to assess the mechanical properties at operating temperatures, the Cu-Nb composite will be investigated by high temperature nanoindentation. The high temperature experiments will be carried out in-situ to obtain the maximum temperature at which the Cu-Nb composite can be used. Significant outcomes will be a fundamental understanding of the microstructural stability and the mechanical behaviour of this novel nanocomposite at elevated temperatures. Furthermore, in order to identify the governing deformation mechanisms at elevated temperatures, the strain rate sensitivity (SRS) and apparent activation volume (AV), will be investigated. The high temperature nanoindentation testing will be realised at the Department of Nuclear Engineering at the University of California Berkeley, USA.

2 Theoretical principles

2.1 High pressure torsion

The high pressure torsion (HPT) process is a well-known and recognized process of severe plastic deformation (SPD) and has been studied in various recent research activities, for example [3, 14-17]. In the HPT process the material is compacted under a high pressure between two plungers via a hydraulic mechanism [3, 14]; a schematic view is shown in Fig. 2.1. As starting material, for example, bulk materials [15, 16] or powders [17] can be used. The plungers are made out of commercial steel. The upper plunger is fixed, while the lower one can perform a torsional rotation with varying revolution speed. Such rotation is exerted after the compressive pressure is applied.

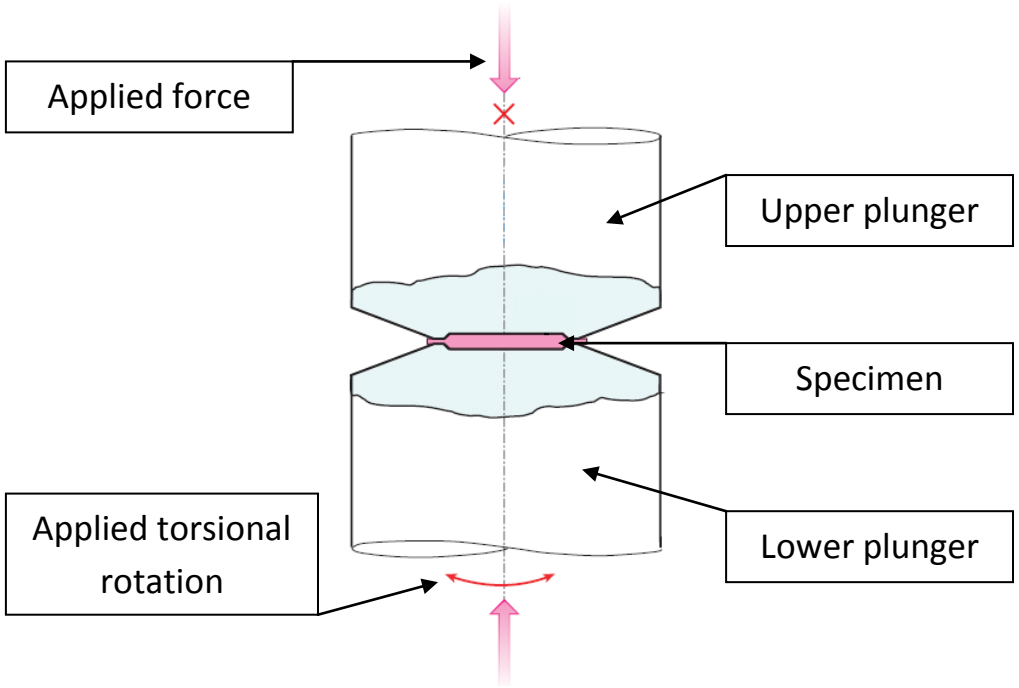

Fig. 2.1: Schematic view of the high pressure torsion process, adapted from [14].

During the HPT process high plastic strains are realized, resulting in fully dense bulk materials with microstructures in the nc and ufg size. The shear strain (γ) can be calculated with equation 2.1 [14], whereas n is the number of revolutions, t is the thickness of the sample after the deformation and R is the distance from the torsion axis (the radial centre position).

$$\gamma = \frac{2\pi n}{t} \cdot R \qquad \text{(Eq. 2.1)}$$

The equivalent plastic strain ($\varepsilon_{\mathrm{pl}}$) of the HPT process is determined by equation 2.2 [14].

$$\varepsilon = \frac{\gamma}{\sqrt{3}} = \frac{2\pi n}{\sqrt{3}t} \cdot R \qquad \text{(Eq. 2.2)}$$

The HPT samples are disc-shaped (as shown in Fig. 2.2) and are typically in the diameter range of several millimetres, depending on the maximum pressure of the device and the shape of the plungers. In order to characterise the specimens properly, the three fundamental directions are declared as shown in Fig. 2.2.

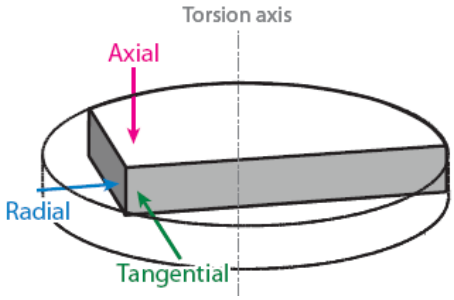

Fig. 2.2: Typical sample received by HPT deformation [14]. The three fundamental directions are identified as an axial, a radial and a tangential direction.

The most important and most investigated direction is the radial direction, whereas R is the distance between the torsion axis (centre of the sample) and the radial position (Fig. 2.3).

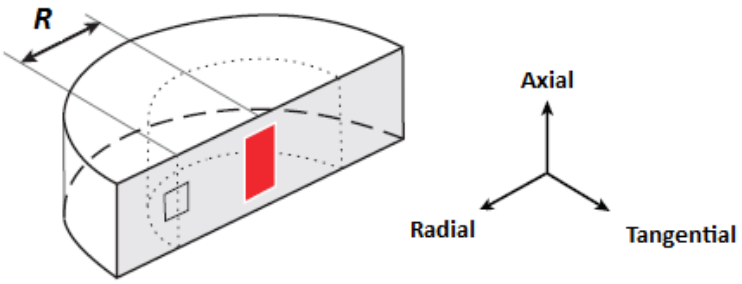

Fig. 2.3: Radial position (R) from the centre of the sample to an outer position [14].

While this technique is very flexible and easy to apply, processing with the HPT approach has also some disadvantages, for example a bimodal distribution of grain sizes and a gradient along the radial direction [3, 14, 15]. In order to create a Cu-Nb composite in the nanorange (nc or ufg) with the smallest possible gradient along the axes, two different processing routes were used, as will be described later.

2.2 Nanoindentation

A possible way to investigate mechanical properties in small dimensions is offered by the instrumented indentation technique, also known as *nanoindentation*. The name nanoindentation is derived from the small penetration depths ranging to the submicron range. With this testing technique the applied load and the resulting penetration depth are recorded simultaneously in load – displacement curves, as shown schematically in Fig. 2.4. The application area of nanoindentation ranges from thin film testing to highly localized measurements of specified phases in composites as well as in other material classes, e.g. ceramics and polymers [18].

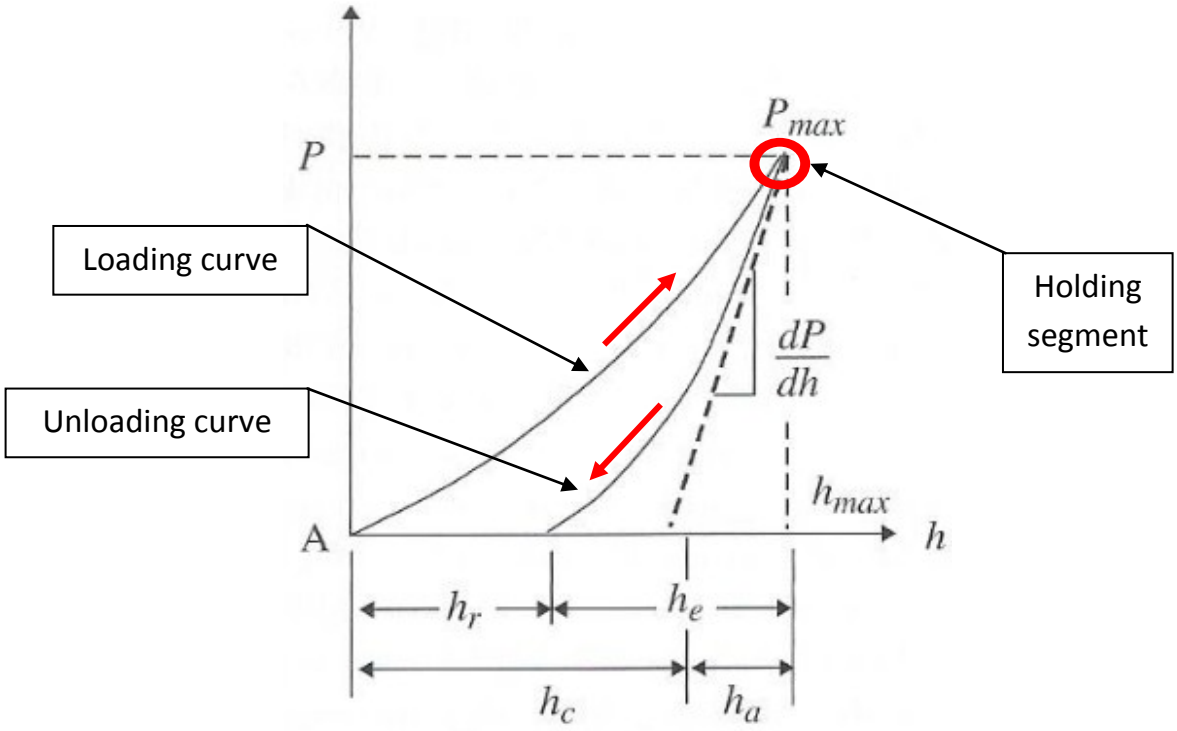

Fig. 2.4: Load – displacement curve as obtained from instrumented indentation testing [18].

In the last years two different approaches were established to perform high temperature nanoindentation testing in order to perform highly localized measurements at elevated temperatures. The central issue is to minimize the thermal drift between sample and indenter tip in order to achieve repeatable and reliable results [19]. One possibility to measure at higher temperatures is to bring a heatable sample and a non heatable indenter tip in contact and independently wait for thermalisation [20]. The second possibility is to heat the sample and the indenter tip to the same temperature [21, 22]. The thermal drift can be adjusted by an isothermal contact to a minimum, thus reliable experiments are possible [23].

The load – displacement curve (Fig. 2.4) is the main output of the instrumented indentation technique, and is divided into the loading part (contains elastic and plastic deformation), a holding segment at maximum load, and an unloading part (assumed to be completely elastic). The Oliver-Pharr method is used for the elastic modulus and hardness determination from the unloading curve. A detailed explanation of this method will not be given in this work, but can be found for example in [18, 19]. Nonetheless, a brief description is summarized in the following part. According to equation 2.3 the hardness (H) of the material can be determined by dividing the maximum load (P_{max}) by the contact area (A_{c}).

$$H = \frac{P_{\text{max}}}{A_{\text{c}}} \qquad \text{(Eq. 2.3)}$$

The contact area (A_{c}) and the indentation depth (h_{c}) are related via the tip area function (AF), which is determined by the geometry of the indenter (equation 2.4). For an idealized Berkovich indentation tip geometry the parameter a_0 equals 24.5. With progressing time and use of the indenter, the tip gets more rounded, resulting in a different tip geometry which has to be accounted for as outlined below.

$$A_{\text{c}} = a_0 \cdot h^2 \qquad \text{(Eq. 2.4)}$$

In order to avoid errors in the measurement, a calibration has to be carried out on an isotropic sample with known properties – Young's modulus and Poisson's ratio. A fused silica calibrating sample is often used as reference material to calibrate the tip AF and to determine the fit parameters a, b and c of equation 2.5. The parameter a is usually close to 24.5, the parameter b reflects the tip rounding from the ideal shape [18, 19].

$$A(h_{\text{c}}) = a \cdot {h_{\text{c}}}^2 + b \cdot h_{\text{c}} + c \cdot {h_{\text{c}}}^{1/2} + \ \ldots \qquad \text{(Eq. 2.5)}$$

In this work the calibration of the tip AF was calculated with equation 2.6. This simplification from a more complex polynomial function to a quadratic equation can be made due to the fact that the term ${h_{\text{c}}}^{1/2}$ has no pronounced influence on the fitting parameter c.

$$A(h_{\text{c}}) = a \cdot {h_{\text{c}}}^2 + b \cdot h_{\text{c}} + c \qquad \text{(Eq. 2.6)}$$

Furthermore, an analytical determination of the Young's modulus is possible, when considering A_c and the contact stiffness (S), as well as the geometry factor (β), which in the case of a Berkovich indenter is 1.034. According to equation 2.7 the reduced modulus (E_r) of the sample can be determined, which reflects the combined modulus of sample and tip.

$$E_r = \frac{\sqrt{\pi}}{2 \cdot \beta} \cdot \frac{S}{\sqrt{A}} \qquad \text{(Eq. 2.7)}$$

With this reduced modulus and equation 2.8 the Young's modulus of the sample (E_s) can be determined. The required parameters are the Poisson's ratio of the sample (ν_s) and the properties of the indenter (ν_i and E_i).

$$\frac{1}{E_r} = \frac{(1-\nu_s{}^2)}{E_s} + \frac{(1-\nu_i{}^2)}{E_i} \qquad \text{(Eq. 2.8)}$$

The measurement of further mechanical properties, for example fracture toughness, residual stress and the strain hardening index (the inverse of the strain rate sensitivity), with nanoindentation techniques is possible [18]. Several techniques have been investigated to measure the strain rate sensitivity (SRS), also referred to as m-value, with nanoindentation. The SRS is described by equation 2.9 as the ratio between the natural logarithmic hardness and the natural logarithmic strain rate, whereat the temperature has to be kept constant.

$$m = \left(\frac{\partial \ln(\sigma)}{\partial \ln(\dot{\varepsilon})}\right)_T \approx \left(\frac{\partial \ln(H)}{\partial \ln(\dot{\varepsilon})}\right)_T \qquad \text{(Eq. 2.9)}$$

The hardness is calculated by equation 2.3; the strain rate ($\dot{\varepsilon}$) is determined as the ratio of the displacement rate ($\dot{h}$) to the displacement (h), as can be seen from equation 2.10.

$$\dot{\varepsilon} = \frac{\dot{h}}{h} \qquad \text{(Eq. 2.10)}$$

The most promising methods to ascertain the SRS are the constant rate of loading (CRL) method proposed by Mayo and Nix [24], the strain rate jump tests reported in [25, 26], the constant strain rate (CSR) method suggested by Lucas and Oliver [27, 28], and the constant load (CL) method recommended by Mayo et al. [29, 30].

The methods that can be carried out on the nanoindentation facility used in this work are the CSR and the CL method, and thus will be discussed next. To obtain SRS values from CSR measurements, hardness and strain rate pairs are required over at least two orders of magnitude on the strain rate axis, as can be seen in Fig. 2.5, in order to have meaningful results [19]. During a CSR measurement the strain rate of the loading is kept constant, which is realised by an exponential loading segment. The strain rate is adjusted by a proportional constant (k) that shows the ratio between the loading rate ($\dot{P}$) and the applied load (P). The strain rate results from the constant k divided by the factor two [19].

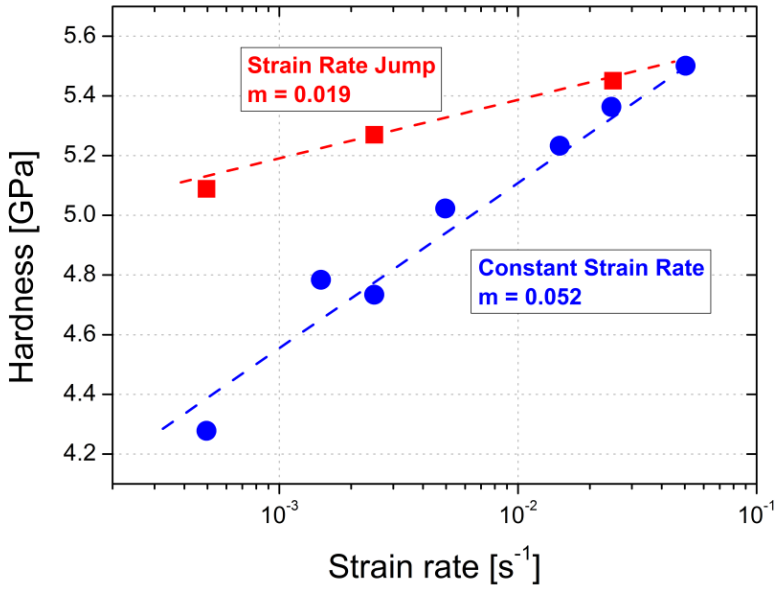

Fig. 2.5: Hardness – strain rate diagram: strain rate jump tests (red data) compared to constant strain rate (CSR) tests (blue data) on nc Ni showing higher values for CSR results [19].

Fig. 2.5 implicates that higher SRS values are observed in the CSR method (blue) than for strain rate jump tests (red) in the case of nc nickel (Ni) [19]. The disadvantage of the CSR method is the high amount of indents needed for a statistical analysis of the obtained data.

The second method to measure the SRS is the CL method. According to Mayo et al. [24] for the CL method less indents are necessary, resulting in a smaller required area on the sample, due to the fact that only one indent with a constant load is needed. The SRS values from the CL method are obtained from the holding segment at maximum load [31]. According to Peykov et al. [31] a graph with *constantly changing strain rate and hardness pairs* is used to calculate the SRS. The curve is then divided into two different stages. Peykov et al. indicated the two stages to *Stage I* and *Stage II* (Fig. 2.6). The CL method will be discussed in chapter 4.3.4 more in detail.

Furthermore, Peykov et al. reported a good agreement between the results obtained from CSR measurements (red dotted line) and the findings of *Stage I* from CL tests (black squares). The data from *Stage II* exhibits higher SRS values [31].

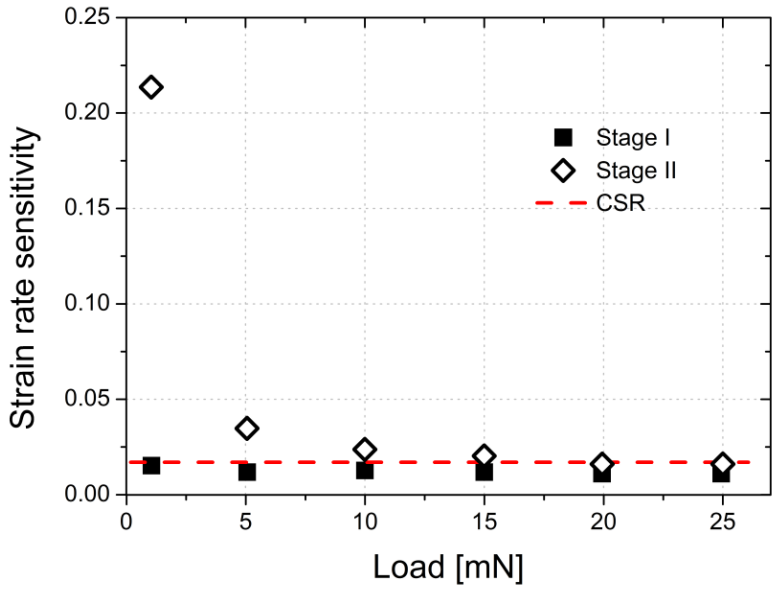

Fig. 2.6: Comparison of the CSR and the CL method for bulk Cu, whereat CSR results and CL *Stage I* measurements exhibit nearly the same SRS, taken from [31].

A second parameter for determining the governing deformation mechanism, the activation volume of the process governing plastic flow (V^*), can be calculated according to equation 2.11 [19] and equation 2.12 [32]. The activation volume is an indicator for the deformation dynamics. The required parameters are the Boltzmann constant (k_B) and the absolute temperature (T). The difference between these two equations will be discussed in chapter 5.3.2.

$$V^* = \sqrt{3} \cdot k_B T \cdot \left(\frac{\partial \ln(\dot{\varepsilon})}{\partial \sigma}\right)_T \qquad \text{(Eq. 2.11)}$$

$$V^* = \sqrt{3} \cdot k_B T \cdot \frac{3}{m \cdot H} \qquad \text{(Eq. 2.12)}$$

In order to illustrate the activation volume, it is often divided by the elemental atomic volume governing the characteristic deformation process, which is here assumed to be the cubed Burger's vector (b) b^3, giving a measure of the number of unit cells involved in the rate limiting step for plastic deformation.

The activation energy (Q_c) of plastic deformation can be determined by equation 2.13 [32].

$$\frac{H}{E} = G \cdot e^{-\frac{Q_c}{RT}} \qquad \text{(Eq. 2.13)}$$

Therefore, the activation energy can be determined by a graphical analysis, where the natural logarithm of the hardness divided by the elastic modulus on the ordinate and the reciprocal absolute temperature on the abscissa is plotted in a diagram. The slope of the curve multiplied by the general gas constant (R) represents the activation energy (Q_c) of the plastic deformation, whereas G is a constant factor.

2.3 Material behaviour

A polycrystalline Cu-Nb nanocomposite has not been reported yet in literature. In order to be able to discuss the results obtained in this work, the material behaviour and some general properties of comparable materials were studied. Hereby, the focus was set on the fcc element Cu. On the one hand this is due to the fact that Cu is extensively studied by several research groups all over the world, and because on the other hand that information about the bcc element Nb is unfortunately very scarce.

Because of the goals of this work (the processing of a composite with small structure sizes and high thermal stability), focus was set on properties as a function of grain size and as a function of temperature.

2.3.1 Young's modulus

In Fig. 2.7 the Young's modulus of Cu, Nb and a Cu-Nb composite as a function of temperature are shown. The data for Cu (orange) and Nb (silver) are taken from [33]. The fcc material Cu has a higher modulus at room temperature (RT) compared to the bcc material Nb.

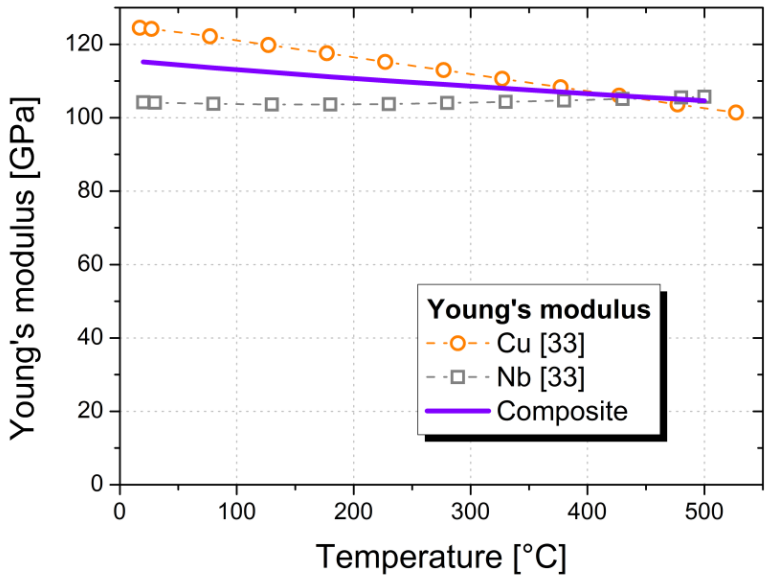

Fig. 2.7: Calculated Young's modulus of a Cu-Nb composite from data according to [33].

A significantly decrease over temperature is apparent in the case of Cu, whereas the changing of the Young's modulus of Nb is negligible. The composite data (violet) was calculated by a rule of mixture using 50% volume fractions of the elements and the data from [33].

According to this calculation the Young's modulus of the composite should decrease with higher temperature as it is often reported for metals [34]. The decrease of the modulus is assumed to be not more than 10% of the value at RT compared to the modulus at 500°C and therefore plays not a significant role. The Young's modulus of the nanocomposite investigated in this work should exert a similar behaviour.

2.3.2 Hardness

As mentioned in chapter 1, Cu-Nb composites have been studied in recent publications. In Fig. 2.8 hardness value results as a function of grain size at RT are plotted from several research groups. The materials shown in this figure are processed via different routes (e.g. sputter deposited multilayered composites or cold drawn wires) and in the range of microstructural feature from ~ 10 nm to ~ 100 nm. Furthermore, not only different types of Cu-Nb composites (green) [5, 8, 9, 10] are shown, also pure Nb (silver) [25] as well as pure Cu (orange) [35] with different grain sizes. The Cu-Nb composite investigated in this work should possess a microstructure size and hardness in this range.

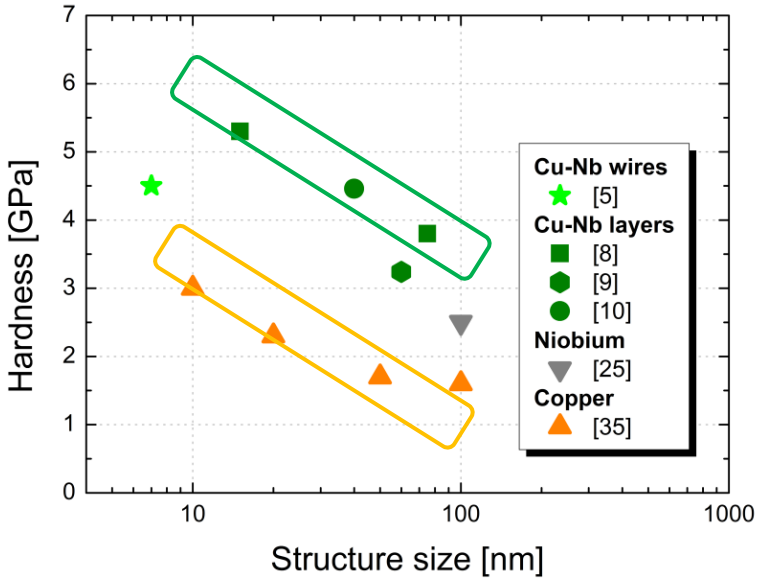

Fig. 2.8: Comparison of RT hardness values from different previous works for pure Cu, pure Nb and Cu-Nb composites. Hall-Petch scaling law indicated in coloured frames.

A scaling relationship (Hall-Petch scaling law) for pure Cu and the multilayered Cu-Nb composite is obvious in Fig. 2.8. Furthermore the diagram shows that Cu-Nb composites possess

higher hardness (~ 2 times higher) than pure Cu and (~ 1.5 times higher) than pure Nb. This aspect can be related to the formation of supersaturated solid solutions during mechanical alloying and small grain sizes in the case of Cu-Nb wires [5]. In the case of Cu-Nb multilayered composites higher hardness values are related to the nanoscaled layers (work hardening in confined layer slip model valid until 500°C). A further contribution results from the interface between Cu and Nb, which acts as a barrier to dislocations because of the different crystallic systems [9].

In Fig. 2.9 the RT hardness as a function of annealing temperature is shown for three different Cu materials differing from each other in microstructure size. The microhardness was determined after annealing at the certain temperature.

The highest hardness is obtained for the nc Cu (brown) [36], followed by the ufg Cu (red) [37] and the coarse grained (cg) Cu (orange) [38] at RT. The Hall-Petch law can be seen at RT as well as at elevated temperatures. Hardness values as a function of temperature of pure Nb were not available in the literature.

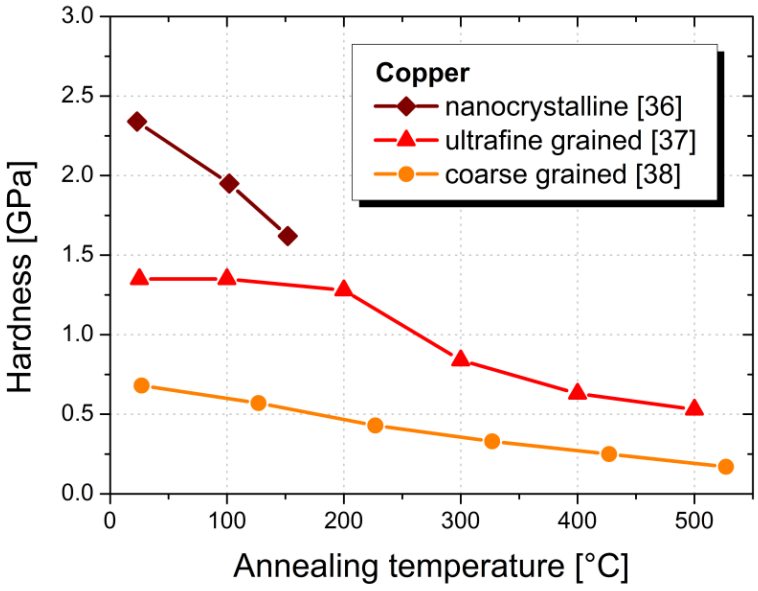

Fig. 2.9: RT hardness as a function of annealing temperature for different Cu microstructures.

The hardness of the nc Cu immediately starts to decrease with increasing temperature. At approximately 300°C a decrease in the hardness of ufg Cu is apparent. This is caused by a grain growth of the fine nc and ufg grains during heat treatments (recovery and recrystallization) as discussed in [37]. The hardness of ufg and cg Cu shows above 300°C a similar trend, nevertheless a huge difference between the ufg and the cg material is obvious.

Microhardness measurements were carried out after annealing treatments at high temperatures in order to study the thermal behaviour of the Cu-Nb composite. In Fig. 2.10 the hard-

ness over temperature of two different Cu-Nb composites is shown. The curves show a high thermal stability for cold drawn wires (nominal microstructure size of 10 nm to 20 nm) [6] and the Cu-Nb multilayer (nominal layer size of 75 nm) [8] after a short time annealing.

These Cu-Nb composites show no significant influence of heat treatment due to the fact that after the annealing the hardness values are nearly the same. This indicates a high thermal stability of Cu-Nb composites, although it has to be kept in mind that only a short time annealing was carried out.

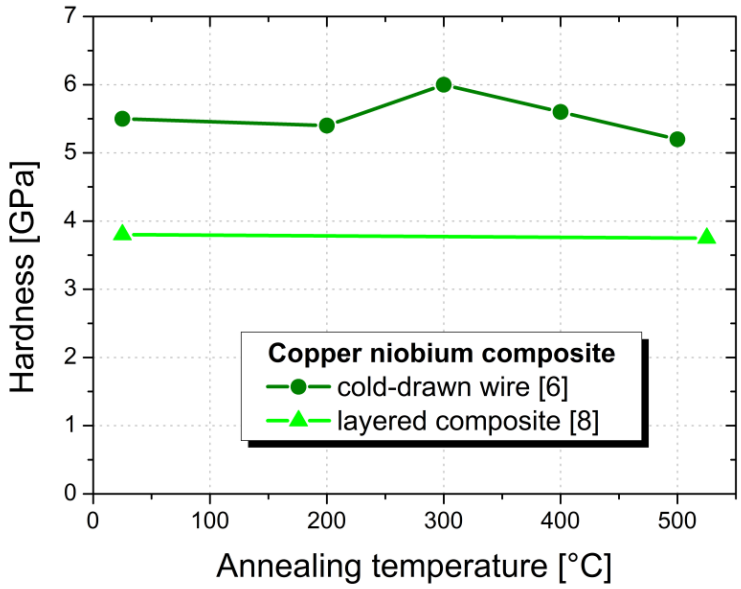

Fig. 2.10: Room temperature microhardness at different annealing temperatures for Cu-Nb cold-drawn wires and Cu-Nb multilayered composites indicating the thermal stability of Cu-Nb materials.[1]

Long time annealing tests were reported for cold drawn wires for 10 hours at 1000°C, whereas the microstructure size increased from ~ 10 nm to ~ 50 nm [7]. In the case of the nanolayered composite heat treatments for a maximum time of 60 hours at 700°C showed nearly no influence of long time annealing treatments verified by subsequent microhardness measurements [8]. Tensile tests at higher temperatures from 500°C to 700°C were carried out on a nanolayered composite showing a slight decrease from RT to 500°C [9].

2.3.3 Strain rate sensitivity

In previous investigations higher strain rate sensitivity (SRS) values were observed when reducing the grain size down to the ufg and nc regime for fcc metals [35, 39]. This can be seen in Fig. 2.11 for Cu as a representative fcc material. In the diagram a transition region is ap-

[1] Explanatory notes: In Fig. 2.10 the thermal stability of the Cu-Nb nanocomposites is only shown to an annealing temperature of approximately 500°C, although higher annealing temperatures were investigated.

parent, approximately at the beginning of the ufg range (d = 500 nm). Below this transition grain size the SRS rises significantly to higher values for nc materials.

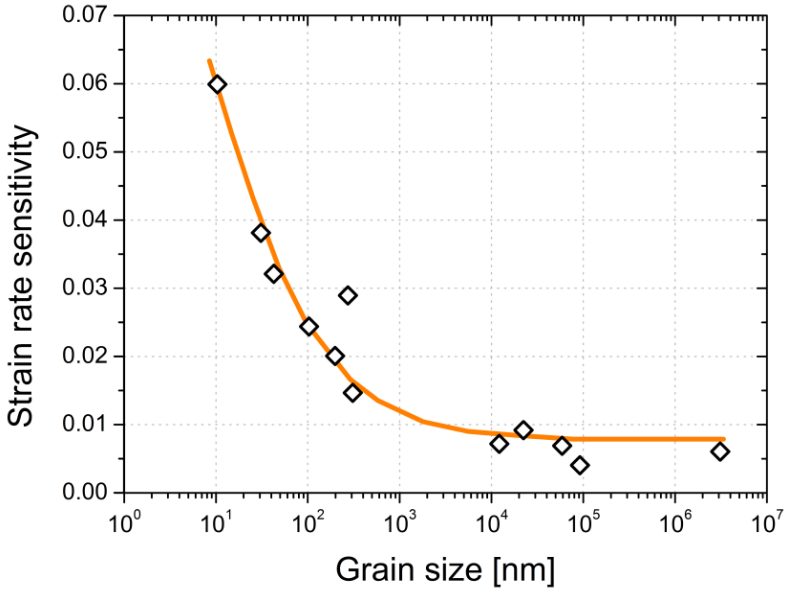

Fig. 2.11: Increase of the SRS with decreasing grain size for Cu, adapted from [35].

An opposite trend was observed for bcc metals, as shown in Fig. 2.12. With decreasing grain size the SRS values are getting lower. Furthermore there is no *take-off* in the ufg region apparent, as compared to Fig. 2.11.

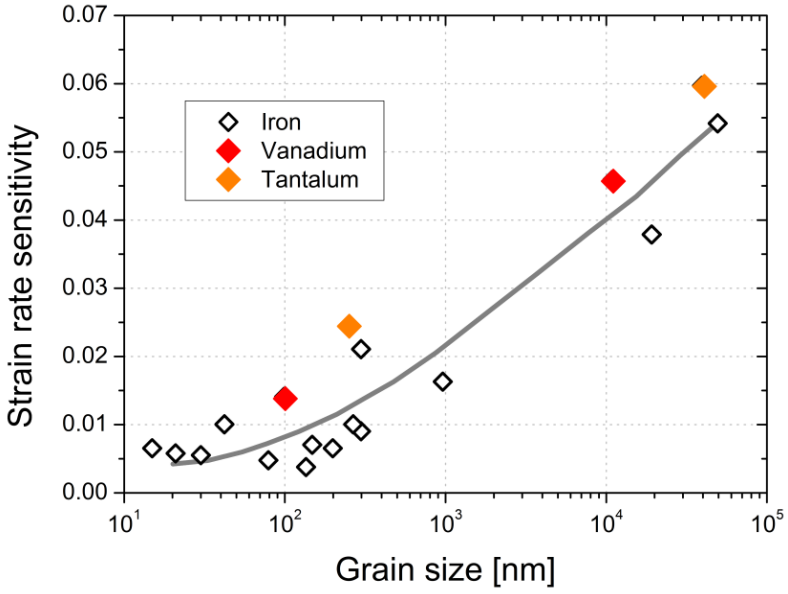

Fig. 2.12: Decrease of the SRS with decreasing grain size in bcc metals, adapted from [39].

The SRS of comparable composites has not been investigated yet in literature for RT, although in [9] the SRS of a multilayered composite is determined to be in the range from 0.3

to 0.5 at 700°C. According to Fig. 2.11 for general fcc elements, [37] for ufg Cu, Fig. 2.12 for bcc elements, and [25] for severely deformed Nb, the SRS for a material with a nominal microstructure size in the order of 100 nm to 200 nm should be approximately 0.010 to 0.020.

The SRS as a function of temperature to a maximum temperature of 300°C for ufg Cu is shown in Fig. 2.13 (similar results were observed in the case of nc Ni [40]). According to the reports on Ni a huge difference between a cg material and the nc counterpart in the SRS is obvious. The increase of the SRS over temperature can be attributed to thermally activated dislocation processes at grain boundaries, for example [35, 37].

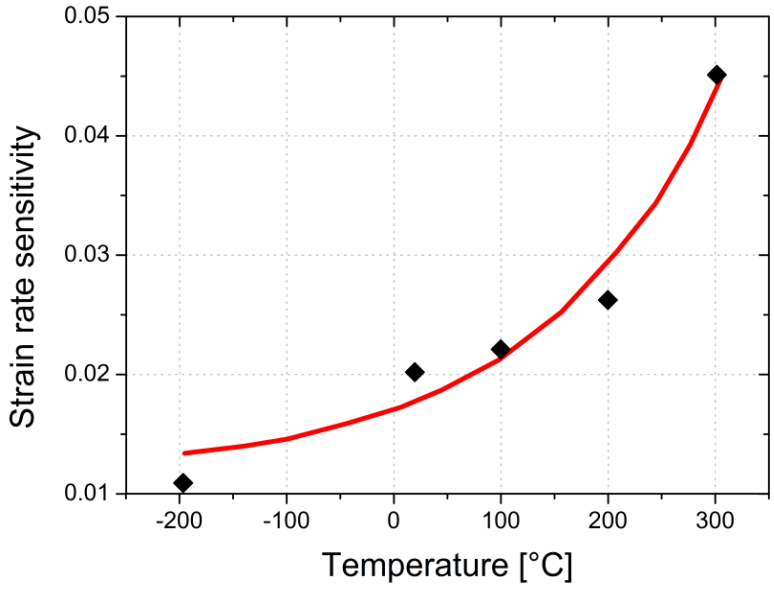

Fig. 2.13: Temperature dependence of the strain rate sensitivity for ufg Cu, adapted from [37].

Because of these literature results, our working hypothesis is that the SRS of the Cu-Nb composite should increase with increasing temperature, showing similar values and a similar trend as reported in the studies of Tao et al. [37] as long as the microstructure is stable.

A recent investigation by Göken et al. [41] on ufg Al showed an increase of the SRS to a certain temperature followed by a decrease. At the beginning the ufg microstructure is stable. At higher temperatures the homogenous ufg microstructure changes to a microstructure with a bimodal distribution where some grains grew significantly.

At the maximum testing temperature the material possesses a coarsened microstructure compared to the initial state (Fig. 2.14). According to these results such drop of the m-value can be related to *the fact that the thermal stability of the material has been exceeded* [41].

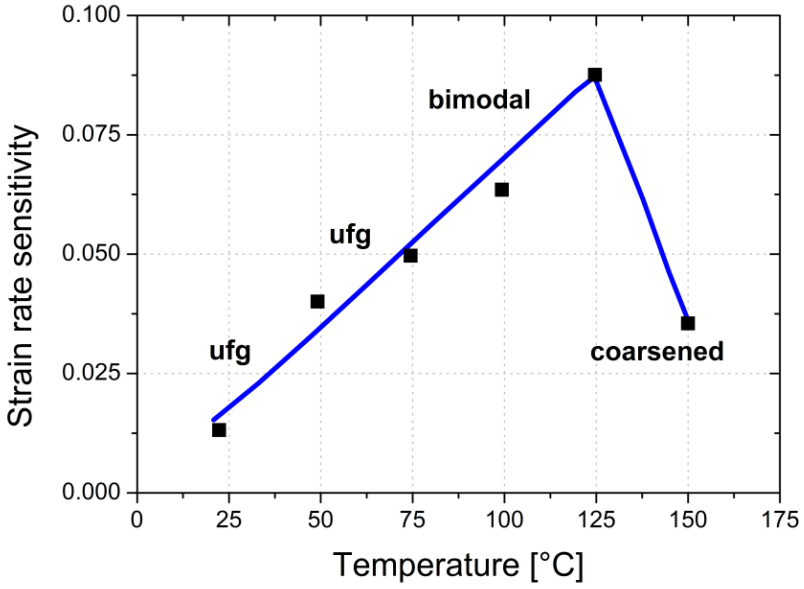

Fig. 2.14: Strain rate sensitivity as a function of temperature for ufg Al, adapted from [41].

With view to the thermal stability of the investigated Cu-Nb composite, a drop in the SRS over temperature could be associated with coarsening of at least one of the two phases. Due to the fact that Cu is the element with the lower melting point compared to Nb (Fig. 1.1), it is assumed that the Cu grains would coarsen first.

2.3.4 Activation volume

For cg materials the deformation mechanisms are well investigated. In table 2.1 the plastic deformation mechanism as well as rough estimates of the corresponding range of the activation volume is represented [3].

Table 4.18: Activation volume and corresponding deformation mechanism for cg materials.

Deformation mechanism	Order of magnitude
Dislocation interaction processes	100 – 1000 b^3
Grain boundary processes	10 – 100 b^3
Diffusion processes	1 – 10 b^3

According to previous observations, for example [35], the activation volume decreases with decreasing the grain size of the material, whereas the governing deformation mechanism (e.g. dislocation interaction processes) remains the same (Fig. 2.15).

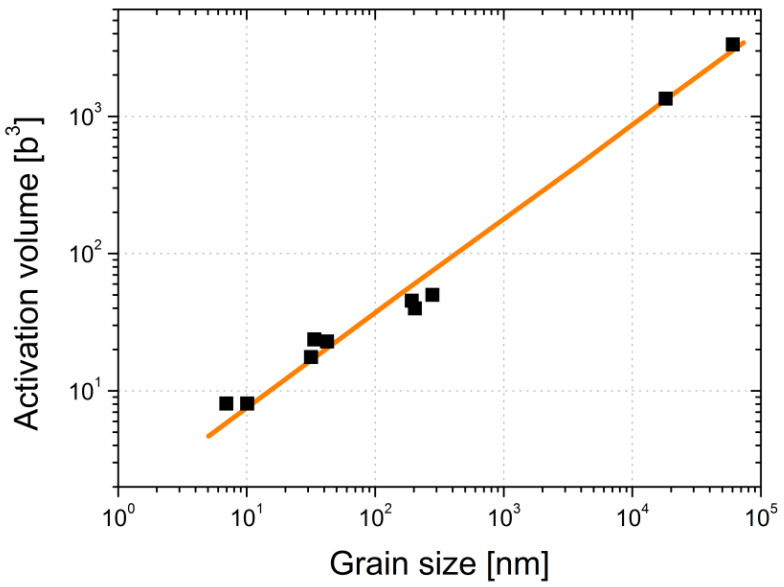

Fig. 2.15: Activation volume in dependence of the grain size for nc Cu, adapted from [35].

The activation volume of Cu with a microstructure size in the ufg range ($\sim$ 100 nm) is approximately 40 b^3, as can be seen in Fig. 2.15. The primary deformation mechanism (dislocation slip) is still the same at smaller structure sizes, but not longer rate governed by the interaction and the cutting of forest dislocation, as proposed in the cg range. Rather, the dominating deformation process in the ufg range for fcc materials (Cu as representative material) is assumed to be a dislocation interaction between glissile dislocations and subgrains and grain boundaries [35, 37]. Other possibilities were discussed in literature, as for example grain boundary sliding [3, 37, 41] and grain boundary rotation [3].

3 Materials and Methods

3.1 Sample preparation

The material investigated in this work was obtained by several processing steps. In the beginning a commercial Cu powder (99.9% purity, particle size in the range from 40 µm to 80 µm) and a Nb powder (99.8% purity, particle size smaller than 45 µm) were mixed together at room temperature (RT) for 60 minutes. The micrometer sized powder mixture contained equal amounts of both powders, respectively 15 g, resulting in a composition with 50 wt.% Cu and 50 wt.% Nb. The atomic percentage is 41 at.% Nb and 59 at.% Cu, whereas the volume percentage is 49 vol.% Cu and 51 vol.% Nb.

After mixing of the two powders, it was necessary to create a fully dense bulk material with a microstructure in the nc or ufg range. The HPT technique was used to create such a composite with a fine microstructure in the order of 100 nm from the powder mixture.

3.2 High pressure torsion

The HPT process was performed on two HPT machines. The *small* HPT machine has a maximum pressure of 40 tons (400 kN), where two plungers measuring 40 mm in diameter were used, as shown in Fig. 3.1. The plungers were sandblasted prior to deformation to ensure a high friction through microroughness and a clean surface [14]. The specimen received is disc-shaped, measuring approximately 8 mm in diameter and 0.6 mm in height.

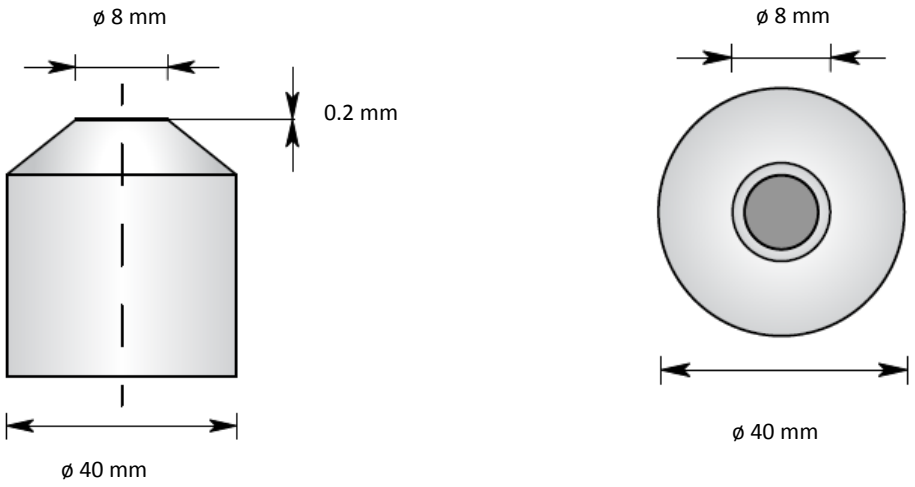

Fig. 3.1: Schematic view and dimensions of the plungers from the *small* HPT tool.

The *large* HPT machine has a higher nominal pressure of 400 tons (4000 kN). The two plungers are also bigger compared to the small one, measuring 150 mm in diameter (Fig. 3.2). The

specimen geometry is nearly the same as in the other case, but again with larger dimensions. The obtained sample measures around 35 mm in diameter and 7 mm in height.

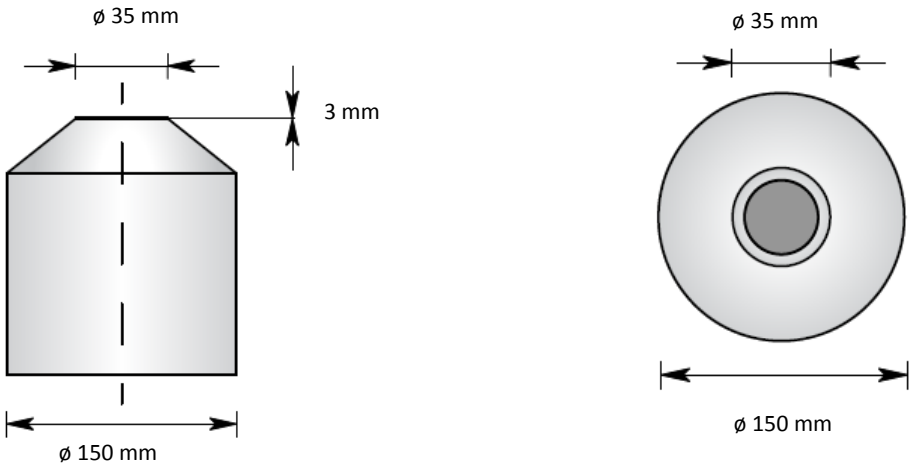

Fig. 3.2: Schematic view and dimensions of the plungers from the *large* HPT device.

3.2.1 One step HPT process

One of the two processing routes is the common HPT process, as described in chapter 2.1. In this work this HPT process is termed *one step* HPT process. In order to retain the powder in the right position for the HPT process, a Cu ring was positioned on the lower plunger measuring approximately 8.5 mm in diameter and 2.5 mm in height and filled with the powder mixture subsequently. The samples were fabricated with the *small* HPT tool, where the number of revolutions was varied from 60 to 200 to ascertain a possibly fine and saturated microstructure evolution. The rotation speed was set to 0.6 rpm. After the deformation all disc-shaped samples measured approximately 8 mm in diameter and 0.6 mm in height, as can be seen schematically in Fig. 3.3.

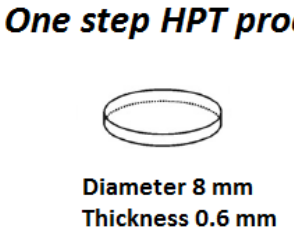

Fig. 3.3: Schematic view of the disc-shaped sample obtained from the *one step* HPT process.

3.2.2 Two step HPT process

A second possible processing route to obtain materials with a microstructure in the nano-range is the so called *two step* HPT process. According to Bachmeier et al. [17], a *two step* HPT process should implicate a more homogenous microstructure and furthermore smaller

grain sizes, because of the higher introduced plastic strains. This two step process starts with pre-compacting of the Cu-Nb powder mixture in the *large* HPT machine, again using an outer ring for filling the powders. The rotational speed was set to 0.067 rpm, the pressure to approximately 200 bar. After ten revolutions a 7 mm high disc, measuring 35 mm in diameter was obtained – the first deformation step was completed. The disc exhibited in the outer regions a macroscopic difference in microstructure compared to the inner regions; this arises from the Cu ring that was used to avoid flow of the powder mixture.

From the disc-shaped sample two rods with a diameter of 7 mm were machined at a radial position R = 2 mm to R = 9 mm. Subsequently, smaller discs (7 mm diameter, 1.1 mm thickness) were cut out of the rods and put into the *small* HPT machine for a second deformation step. This procedure is shown schematically in Fig. 3.4.

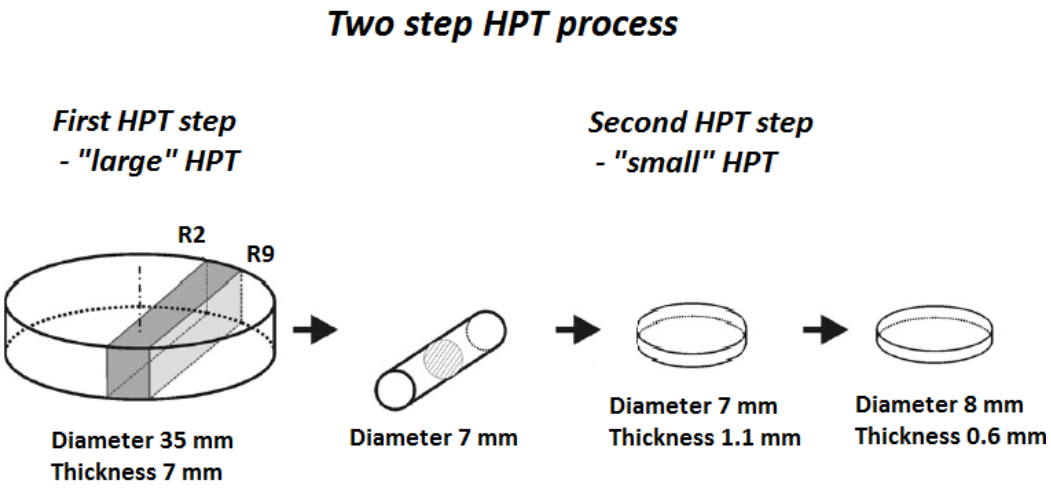

Fig. 3.4: Schematic view of the *two step* HPT process, adapted from [17].

The discs were deformed in perpendicular deformation direction to the first processing step (90° to the first deformation direction) to break down the so-called deformation striations, which are often observed during HPT deformation [17]. In order to investigate the best possible processing, the number of revolutions was varied from 100 to 200. After the second deformation step the specimens had approximately the same diameter as in the *one step* HPT process. The height of the discs were slightly lower, approximately 0.5 to 0.6 mm.

3.3 Heat treatment

In different former investigations Cu-Nb composites in the nc range exhibited high thermal stability during annealing at elevated temperatures (Fig. 2.10). For example, Botcharova et al., discovered a high thermal stability of mechanically-alloyed nc Cu-Nb alloys (micro-

structure size of approximately 50 nm) after annealing for 10 hours at 1000°C [7]. On the other hand, Misra et al. reported in their research study dealing with nanolayered Cu-Nb thin films (microstructure size of 75 nm) a temperature stability for long annealing times at 700°C [8]. In order to ensure a fine grained microstructure that is necessary for the demanded properties of the novel Cu-Nb composite, a thermal stability check is indispensable.

With a view to the structural stability of the Cu-Nb composite at elevated temperatures, which among other things is investigated in this work, a heat treatment was carried out. Beyond that, the annealing is necessary to avoid supersaturated solid solutions, although Cu and Nb are immiscible. Previous investigations showed that even immiscible elements can form saturated solutions, according to [17, 42], due to mechanical intermixing during HPT processing. The mixing depth was assumed to be in the range of several nanometres at the interfaces (grain boundaries) of the two elements.

The samples were heated in a XERION vacuum furnace at 500°C for 60 minutes. During the whole heat treatment (heating, holding, cooling) the furnace was consistently under a vacuum of at least $3 \cdot 10^{-4}$ mbar. The temperature profile is shown in Fig. 3.5.

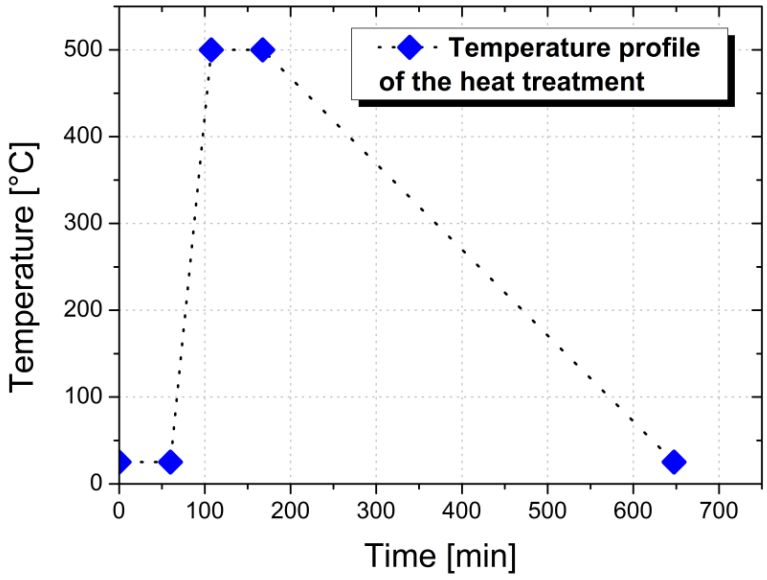

Fig. 3.5: Temperature profile of the heat treatment of the composite after HPT deformation. The first segment indicates the establishing of the vacuum.

The first holding segment in Fig. 3.5 is for establishing the vacuum; the heating rate of 10°C per minute was adjusted. After the heat treatment at 500°C the specimens were slowly cooled in the vacuum furnace to RT without a specific cooling rate.

3.4 Microindentation hardness testing

3.4.1 Experimental setup

In order to assess the homogeneity of the produced samples and an estimation of the strength of the composite after the different HPT processes, microhardness measurements were carried out. The aim was to investigate the homogeneity in the radial direction [15] of the sample (Fig. 2.2). The measurements were made on a BUEHLER Micromet 5100 using a diamond Vickers indenter.

The testing load was set to 500 gf, resulting in an indent size in the range from 40 to 60 µm, depending on the radial position, respectively the material hardness. A distance between each indent of 250 µm was kept constant along the radial direction to avoid any interaction between deformed volumes.

3.4.2 Sample preparation for microindentation

To investigate the homogeneity, the hardness of the HPT samples was measured in the radial direction after the deformation and a subsequent heat treatment. Therefore, the specimens were cut in the radial direction into two pieces and embedded on a STRUERS Pronto-Press-10 in PolyFast, a phenolic hot mounting resin with carbon fillers, at 180°C and a load of 15 kN. The process time was 15 minutes. After the embedding the samples were prepared on a STRUERS TegraPol-11, using a grinding and polishing procedure shown in table 3.1.

Table 3.1: Standard metallographic grinding and polishing procedure.

Disc type	Name		Duration
Grinding disc	Piano	Planar grinding	1 minute
Grinding disc	Largo	1200	4 minutes
Polishing disc	Dac	3 µm	3 minutes
Polishing disc	Nap	1 µm	2 minutes
Polishing disc	Chem	OPS	2 minutes

After the grinding in radial direction (Fig. 2.2) the samples were polished with two different diamond suspensions of 3 µm and 1 µm particle size. The metallographic procedure was finished by polishing with 0.05 µm colloidal silica. The microhardness testing was carried out after this preparation.

3.5 Microstructural characterisation

3.5.1 Sample preparation for microstructural characterisation

For the characterisation by different microscopic techniques, the samples were prepared in the radial direction (Fig. 2.2) following the same procedure as described in chapter 3.4.2. After the metallographic procedure the samples were etched to increase the contrast. The wet etchant consisted of ethanol, iron(III)-chlorid and hydrochloric acid and is usually used for etching Cu samples. The exact composition can be seen in table 3.2.

Table 3.2: Composition of the wet etchant for Cu.

Name	Chemical symbol	Amount	Unit
Ethanol	C_2H_6O	100	ml
Hydrochloric acid	HCl	20	ml
Iron(III)-chlorid	$FeCl_3$	5	g

The maximum etching time should be limited to approximately 10 seconds. An etching duration exceeding this timing results in an etching modification of the surface.

3.5.2 Characterisation by light microscopy

In order to obtain a first overview of the Cu-Nb composite processed by different processing routes as investigated in this work, a microstructural characterisation was performed with a light microscope (LM) subsequently to microhardness measurements in radial direction. Moreover, the microhardness measurements could be visualized.

The characterisation was carried out using an OLYMPUS BX51 microscope. The magnification was set to 200x, whereas a general overview of a HPT sample was carried out with 100x.

3.5.3 Characterisation by scanning electron microscopy

The microstructural characterisation was performed with a scanning electron microscope (SEM) type LEO 1525 using a back scatter detector (BSD). The samples were examined in radial direction in the SEM at different magnifications. The operating voltage was set to 20 kV, the working distance to 6.4 mm. Cu is lighter compared to Nb and should appear darker in the image due to the lower backscattering of electrons. As consequence Nb should appear brighter (Fig. 1.2).

3.6 Nanoindentation hardness testing

3.6.1 Experimental setup

To investigate mechanical properties of the novel Cu-Nb composite in the submicron range as well as time dependent properties, depth sensitive indentation – *nanoindentation* – was used. The testing was performed on a Micro Materials facility shown in Fig. 3.6 (a). Furthermore, this nanoindenter offers the possibility to perform high temperature measurements to a maximal temperature of 700°C. This is achieved by heating the sample as well as the indenter tip to avoid thermal drift. With this nanoindenter in-situ high temperature mechanical properties can be measured. A high temperature setup can be seen in Fig. 3.6 (b) and was described in [23].

(a) (b)

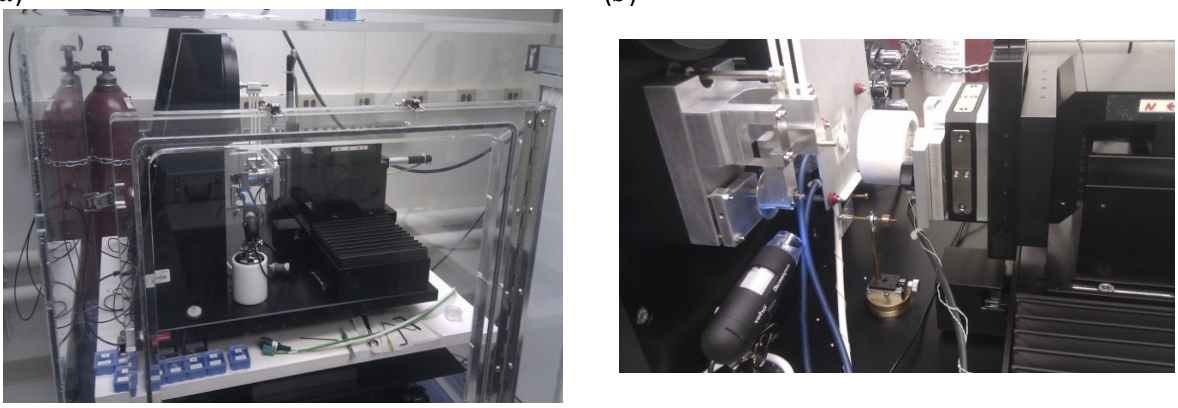

Fig. 3.6: (a) Overview of the Micro Materials nanoindentation facility with the pumping chamber and gas bottles in the background for flooding the chamber. The facility is on a floating table, which is the white board. (b) View of the high temperature setup of the Micro Materials nanoindenter.

In Fig. 3.6 (a) a chamber and gas bottles in the background are visible. The chamber, and hence the nanoindentation experiment, can be purged with gas to bring the oxygen content in the chamber to < 1%. At this point it has to be mentioned that oxidation cannot be totally avoided. The floating table was adjusted in order to minimize the influence by (noise) vibrations of the surrounding.

A more detailed view of the high temperature sample holder (hot stage) and the heatable indenter tip is shown in Fig. 3.7 (a schematic view of both devices can be seen in [23]). In order to determine the optimal measurement position for the indentation tests, a microscope with four magnifications is installed. The heat shield serves as a thermal protection for the connecting wires of the indenter tip. In order to measure at higher temperatures, a water cooling system is indispensable.

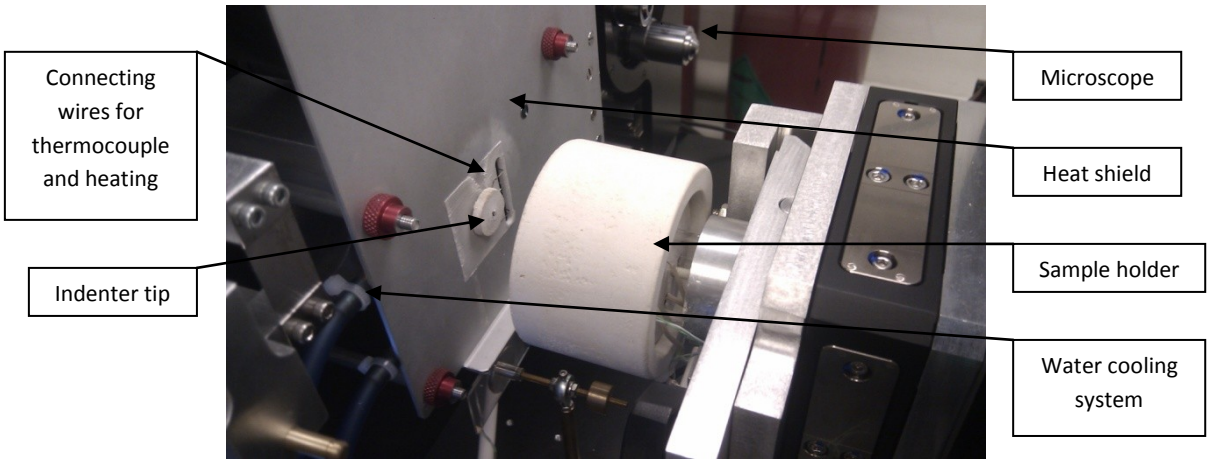

Fig. 3.7: Detailed view of the high temperature setup. The indenter tip and the hot stage, as well as other features as listed above are visible.

The used indenter tips were a heatable cubic boron nitride (cBN) Berkovich indenter for the high temperature experiments and a diamond Berkovich indenter for comparative measurements at RT after the heating experiments. The heatable cBN indenter can be used to a maximum temperature of approximately 700°C. The area function of the indenter was calibrated before and after an experimental run at elevated temperatures on a fused silica sample in order to minimize the influencing factors from tip wearing.

The analysing software is called Nano-Test Platform Three from Micro Materials.

3.6.2 Sample preparation for nanoindentation

The HPT samples were grinded in axial direction (Fig. 2.2) to half of the height, i.e. approximately 250 to 300 µm. This was achieved by measuring the thickness of the sample (height) every 20 seconds while grinding. Afterwards the discs were polished with the same procedure as described in table 3.1 and chapter 3.4.2.

To perform the instrumented indentation testing, the polished samples were mounted on two different sample holders, depending on the temperatures where the measurements should be carried out. In the case of RT measurements, the polished discs were mounted with common super glue on steel sample holders.

In the case of high temperature measurements, the polished specimens were mounted with the high temperature cement OMEGABOND 600 on the hot stage sample holder as can be seen in Fig. 3.8. To measure the surface temperature of the specimen during the heat treatment, a thermocouple was attached to a second identical sample (temperature reference sample) that was mounted right beside the testing sample.

This second sample and the thermocouple wires were fully covered with the high temperature cement. A second thermocouple is installed in the hot stage sample holder [23] and was used for comparative determination of the heating temperature.

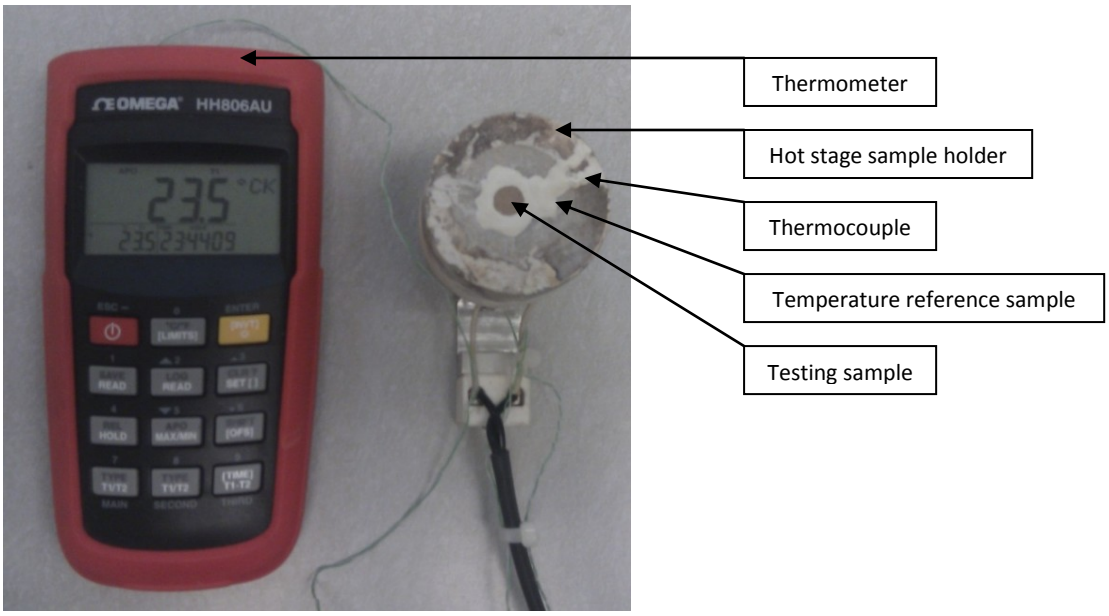

Fig. 3.8: Thermometer, thermocouple and mounted sample on the *hot stage*.

The mounting of the testing sample was difficult due to the fact that a disc-shaped HPT sample is not fully flat on the non polished side. Because of this, a thin layer of cement was put under the sample to ensure planarity to the hot stage sample holder, and hence to the indenter tip.

A usual drying of the cement lasts for approximately 24 hours. By heating up the sample on the hot stage to 60°C for 60 minutes this drying process could be accelerated. Simultaneously, the function of the two thermocouples was tested.

3.6.3 Nanoindentation parameters

The nanoindentation measurements were performed load controlled and depth controlled, whereas the vast majority of the experiments were carried out load controlled. The thermal drift correction was carried out on a load level of 10% of the maximum load, whereas the final 60% of the data of the dwell period for drift correction was used for drift rate calculation (holding segment at low loads in Fig. 3.9).

The thermal drift rate of the unloading curve was determined due to the fact that this part of the load – displacement curve was used for determination of the material properties (Young's modulus). The tests had the following parameters shown in table 3.3 in common.

Table 3.3: General testing parameters for nanoindentation testing.

Parameter	Unit	Value
Limit Stop Load	mN	0.10
Indenter Contact Velocity	µm/s	0.50
Initial Load	mN	0.10
Dwell Period for Drift Correction	s	60

In the case of the load controlled method, the ramp type was set to *fixed time*. Further particulars can be seen in table 3.4. All load controlled measurements, unless otherwise noted, feature the mentioned parameters and vary only in the duration of the dwell period.

Table 3.4: Loading and unloading parameters of load controlled measurements.

Parameter	Unit	Fixed time
Load Time	s	10
Unload Time	s	5

In the case of the depth controlled method, the ramp type was once set to *fixed rate* and the other time to *proportional*. The particulars for the first ramp type as well as the second ramp type are shown in table 3.5. The *proportional* tests were used to perform the CSR measurements. The depth controlled measurements were performed using the shown parameters unless otherwise noted.

Table 3.5: Loading and unloading parameters of depth controlled measurements.

Parameter	Unit	Fixed rate	Proportional
Loading Rate	mN/s	10	-
Unloading Rate	mN/s	20	20
Proportional Constant	1/s	-	0.10

A general schematic overview of the load – time profile is shown in Fig. 3.9 for all three above mentioned testing setups. At the maximum load a holding segment is apparent in all three testing conditions representing the dwell time at maximum load. In order to compare the obtained results the unloading was set in all three experiments to a constant value as indicated in Fig. 3.9.

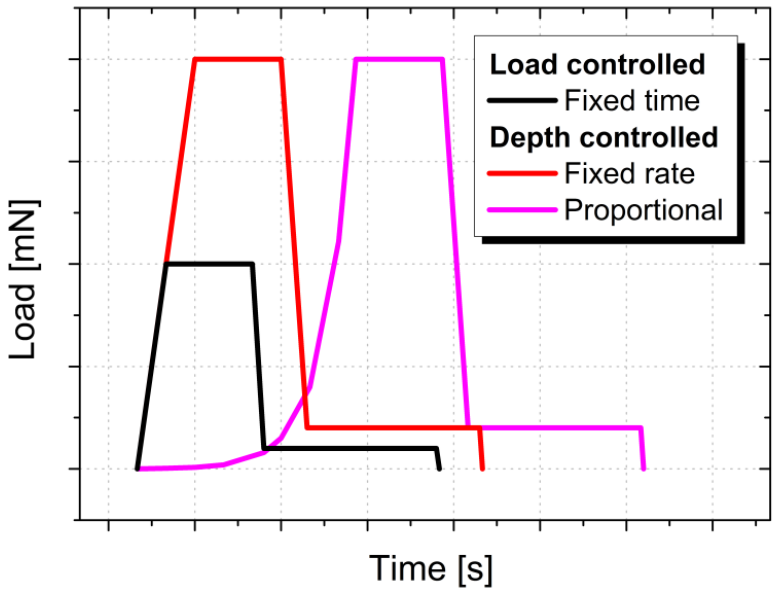

Fig. 3.9: General schematic overview of the three different load – time profiles.

Higher penetration depths are obtained for depth controlled tests. The advantage of depth controlled measurements is that the tested volume is always constant.

3.6.4 Nanoindentation experiments

The measurements were performed in axial direction of the sample at R = 3 mm (Fig. 2.2). A distance of 30 µm was kept constant between the indents to avoid an overlapping of the plastic zones and thus an influence between two adjacent indents.

In order to determine the high temperature mechanical properties of the novel Cu-Nb composite two experimental runs were performed on nominally identical specimens; one starting from RT to a maximum temperature of 300°C termed *first experimental run* (or 1^{st} *run*), and the second starting from 300°C to a maximum temperature of 500°C termed *second experimental run* (or 2^{nd} *run*).

The temperature profile of the first run is shown in Fig. 3.10 (a), the profile of the second one can be seen in Fig. 3.10 (b). The first blue square of each segment marks the beginning point, the second one the thermalisation point and the third one the end point. The specimens were thermalised for at least 60 minutes at each testing temperature from 100°C to 500°C. The temperature dependent measurements were performed in 100°C steps. The heating rate is 1.6 °C per second. After the testing procedure, the sample was cooled to RT without a specific cooling rate.

(a) (b)

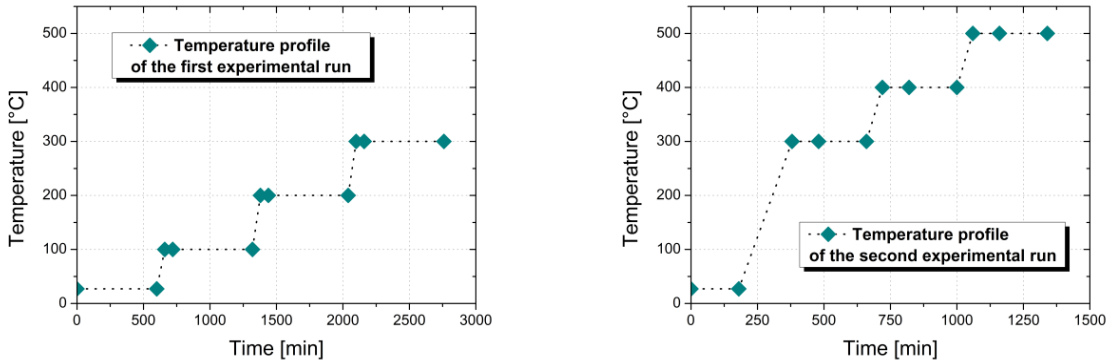

Fig. 3.10: Temperature profile of (a) first experimental run from RT to 300°C and (b) second experimental run from 300°C to 500°C.

In the first experimental run the sample was exposed for around 600 minutes at each testing temperature. Two load controlled (black curve in Fig. 3.9) and three depth controlled (pink curve in Fig. 3.9) sets of indents are performed. Each setting consists of ten indents, resulting in an array (*indent field*) of approximately 120 µm times 270 µm (Fig. 3.11).

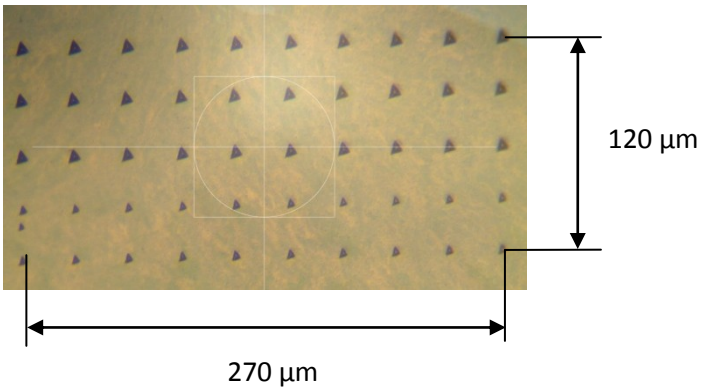

Fig. 3.11: Indent field area showing three depth controlled (first three rows from top) and two load controlled (last two rows at bottom) test runs from RT measurements.

In the second experimental run the sample was kept approximately 300 minutes at each testing temperature. This is due to the fact that only two different indent settings (two load controlled measurements) were performed. As described in the first run, each setting consists of ten indents, resulting in a smaller array size of 30 µm times 270 µm.

4 Results

4.1 Microindentation hardness testing

Microhardness measurements were performed on three specimens, each of them representing a different processing set. The two processing routes (*one step* and *two step* HPT deformation) as well as a different number of revolutions in the *one step* process were investigated. Further microhardness investigations were carried out on heat treated *two step* HPT specimens after an annealing at 500°C for 60 minutes. Table 4.1 summarizes the tested samples.

Tab. 4.1: Overview of samples tested by microhardness measurements.

Sample number	Processing route	Number of revolutions	Heat treatment
# 1	*one step* HPT	60	-
# 2	*one step* HPT	150	-
# 3	*two step* HPT	10 (1^{st} step), 200 (2^{nd} step)	-
# 3	*two step* HPT	10 (1^{st} step), 200 (2^{nd} step)	500°C for 60 min

4.1.1 Influence of the processing route

Equation 2.2 and equation 2.3 indicate higher hardness values for a higher number of revolutions and a higher distance from the torsion centre [15]. In order to investigate the influence of the processing microhardness was measured of different samples.

The first microhardness testing was performed on the *one step* HPT sample with a low number of revolutions (60 revs). The results are shown in Fig. 4.1 by the black curve. Directly beneath the diagram an LM overview of the tested HPT sample is shown (indicated with a black frame). A gradient from the outer regions to the centre is apparent, whereas the decrease is exceeding 50% difference.

At the outer regions of the sample (radial position R = 3.0 mm to R = 4.0 mm) the sample exhibits microhardness values ranging from 420 HV to 500 HV. At the centre position (radial position R = 0.0 mm) the values reach the lowest level of approximately 230 HV.

Additional microhardness measurements were performed on a *one step* HPT sample with 150 revolutions (green) and a *two step* HPT sample with 10/200 revolutions (red). LM overviews are again shown in order to get a feeling of the microstructure. Because of the sym-

metric behaviour of the hardness values, the measurements were performed from the centre point of the specimen to the edge of the sample over a distance of approximately 4 mm.

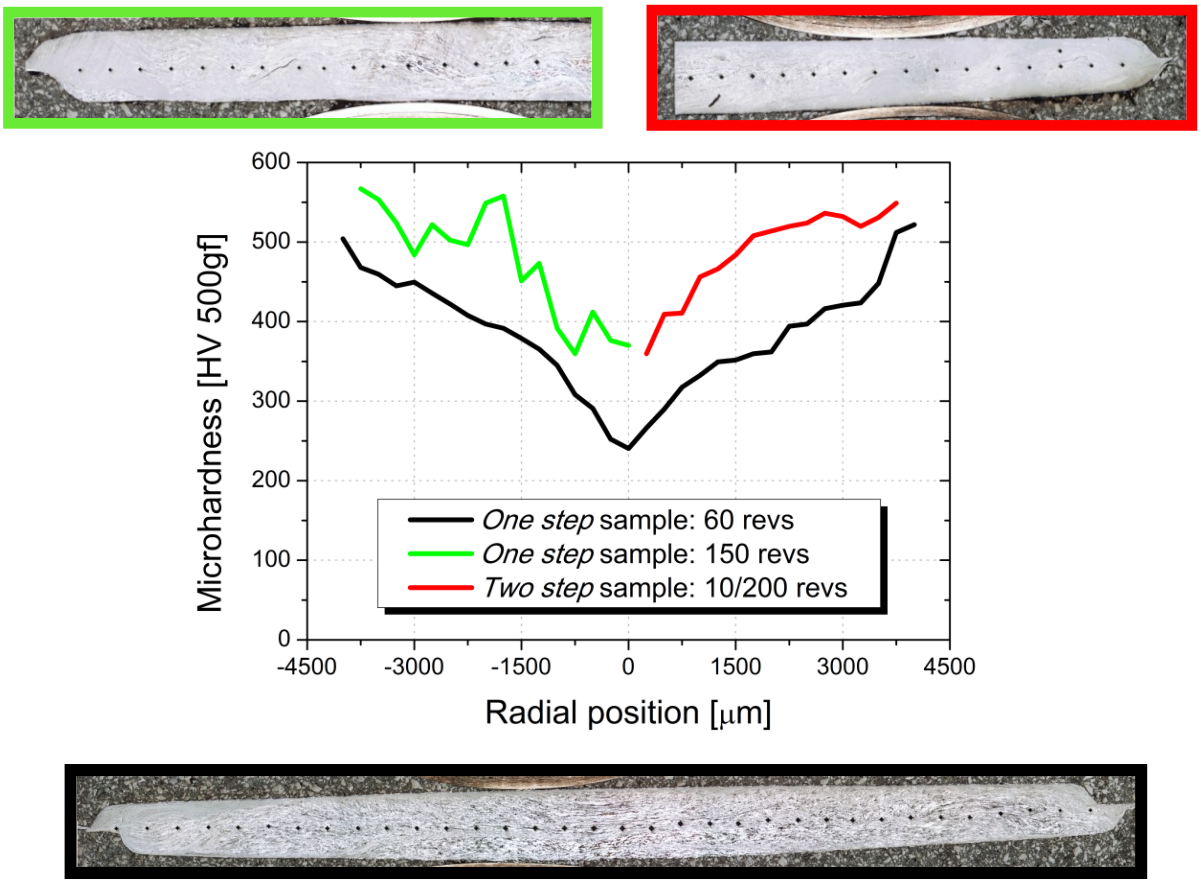

Fig. 4.1: Comparison of microhardness results and light microscopy overviews over the radial position obtained from a *one step* HPT sample with 60 revs (black), a *one step* sample with 150 revs (green) and a *two step* sample with 10/200 revs (red), showing the influence of the processing route.

In the case of the *one step* HPT sample (green) the maximum hardness value is 575 HV at the outer position. At the centre position the hardness shows a value of approximately 380 HV. The lowest hardness value is observed at R = 0.75 mm and is approximately 360 HV. A gradient from the outer to the inner regions is apparent, as well as some scattering of the hardness values occurs.

In the case of the *two step* HPT sample (red) the highest hardness of approximately 550 HV is obtained at a radial position of R = 4.0 mm. A decrease of the hardness values to the centre of the sample is obvious, showing a hardness around 370 HV at R = 0.0 mm.

4.1.2 Influence of the heat treatment

In order to determine the thermal stability of the composite, the microhardness of non heat treated samples as well as heat treated samples was measured. The heat treatment at 500°C

for 60 minutes was carried out on the *two step* HPT samples. The interesting fact is the impact of the heat treatment on the microhardness measurements.

In Fig. 4.2 the hardness values of the non heat treated (red) and the heat treated (magenta) samples are shown. A constant plateau in the range around R = 3.0 mm can be seen. The microhardness values in this area are approximately 525 HV.

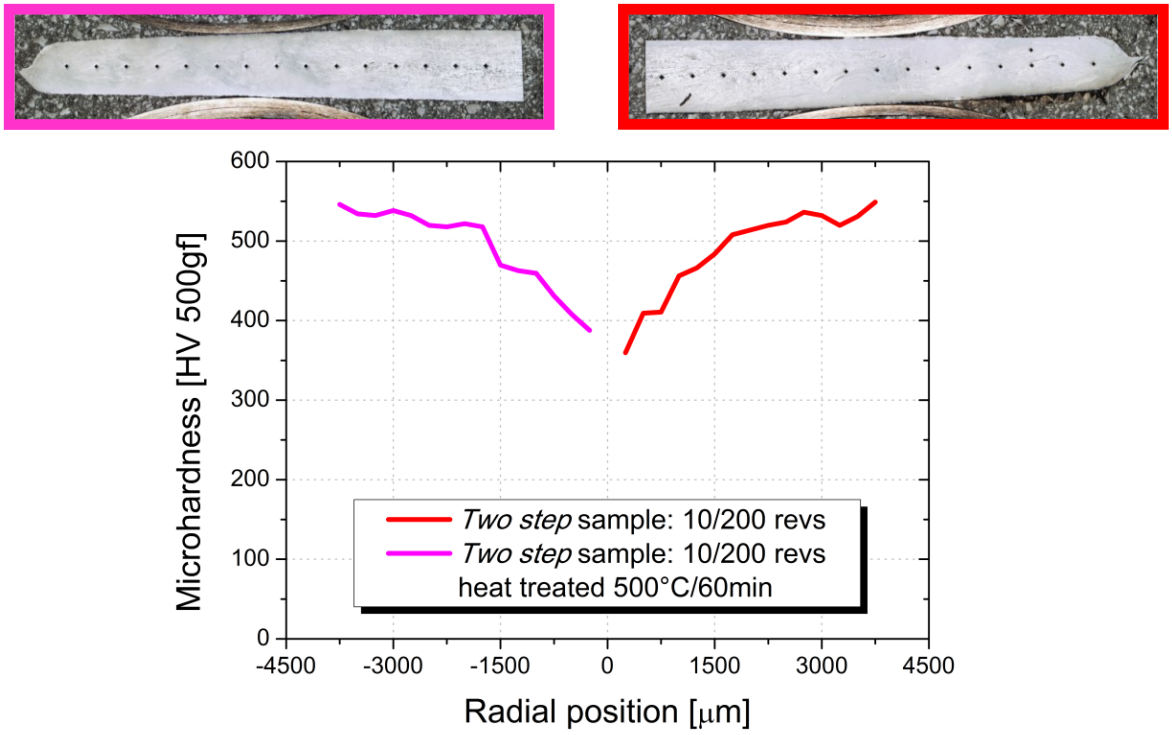

Fig. 4.2: Comparison of microhardness results and light microscopy overviews over the radial position obtained from a non heat treated *two step* HPT sample (red) and a heat treated *two step* sample (magenta) with 10/200 revs, showing no pronounced influence of the heat treatment.

In both cases (non heat treated – red and heat treated – magenta) a gradient from the outer regions to the centre of the sample can be seen. The maximum hardness of 550 HV is nearly the same at R = 4.0 mm for both samples. At the centre position the hardness values are in the range from 390 HV in the case of the heat treated sample, and 370 HV for the non heat treated one.

4.2 Microstructural characterisation

4.2.1 Light microscopy

In order to obtain a first microstructural overview of the Cu-Nb composite processed by different processing routes and investigated in this work, a microstructural characterisation was performed with a light microscope (LM) subsequently to microhardness measurements.

First LM pictures are shown in Fig. 4.1 and Fig. 4.2. A general overview of the microstructure is given in Fig. 4.3, where the whole radial direction of the *one step* HPT sample (60 revolutions) is shown. The centre position (R_0 = 0.0 mm) and a region of interest in the outer regions (from radius R_1 = 2.5 mm to a radius R_2 = 3.5 mm) are indicated.

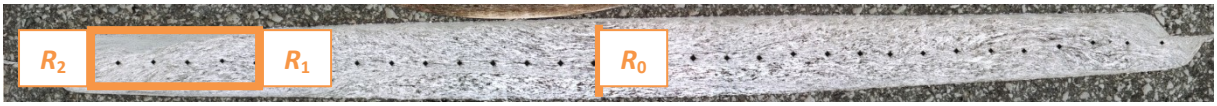

Fig. 4.3: Light microscopy picture of the whole radial sector of a *one step* HPT sample. The centre position (R_0 = 0.0 mm) and an area of interest (from R_1 = 2.5 mm to R_2 = 3.5 mm) are pointed out.

In Fig. 4.4 (a) to (d) LM pictures of the region from R_1 to R_2 are shown for each of the four investigated HPT samples. The pictures were taken with a magnification of 200x.

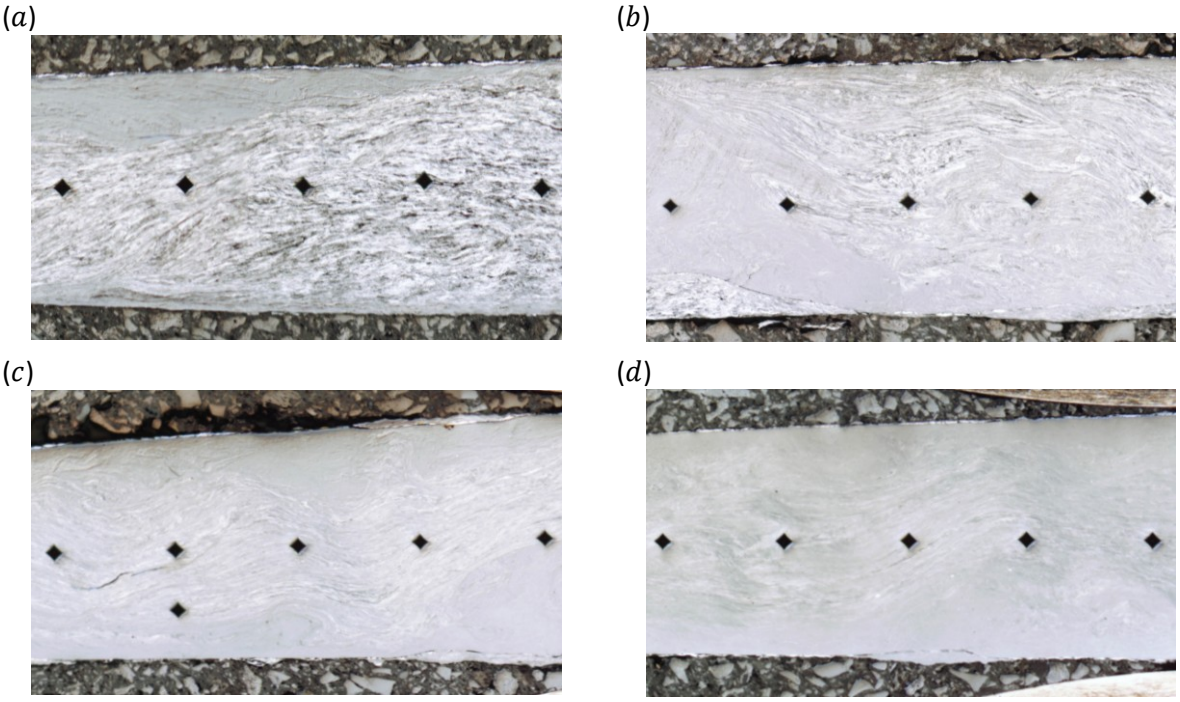

Fig. 4.4: Detailed view from R_1 = 2.5 mm to R_2 = 3.5 mm of a *one step* sample with (a) low number of revs (60 revolutions), (b) high number of revs (150 revolutions), (c) a *two step* sample and (d) a heat treated *two step* sample (10/200 revolutions).

The white and black areas can be related to Cu and Nb. The microstructure is assumed to be coarse due to the fact that it is resolvable with LM and a 200x magnification. Especially in Fig. 4.4 (a) huge areas of a resolvable microstructure can be observed (*one step* HPT sample with 60 revolutions). Only at the top small non resolvable areas are apparent.

Moreover, deformation striations are visible over the whole radial direction. With increasing the number of revolutions to 150 in the *one step* HPT process the microstructure gets finer. Although still striations are apparent, the microstructure is more homogenous compared to the first one as can be seen in Fig. 4.4 (b).

The non heat treated *two step* HPT sample with 10/200 revolutions in Fig. 4.4 (c) exhibits even more non resolvable areas by light microscopy. This is an indication for a fine micro-structure. Cracks are visible due to the high plastic strains that are introduced during a HPT deformation. Notably, the microstructure of the investigated composite does not change after a short time annealing within the resolution limits of the LM, Fig. 4.4 (d).

4.2.2 Scanning electron microscopy

Characterisation of the microstructure

In order to investigate the microstructure of the Cu-Nb composite more in detail the sample was examined by scanning electron microscopy (SEM). SEM techniques were used not only to estimate the nominal size of the composite, but also to look for an appropriate area of approximately 300 µm for the high temperature nanoindentation testing (as was mentioned in chapter 3.6.4).

Fig. 4.5: Area for further SEM investigations on a heat treated *two step* sample.

The pictures were made in the radial direction of the sample in the range from R_1 = 2.8 mm to R_2 = 3.6 mm as can be seen in Fig. 4.5 on the heat treated sample processed via the *two step* HPT process. In Fig. 4.6 (a) to (d) the microstructure of the composite (heat treated *two step* HPT sample with 10/200 revolutions) at four different magnifications ranging from 1,000x to 40,000x at a radius of R = 3.0 mm from the torsion axis is shown.

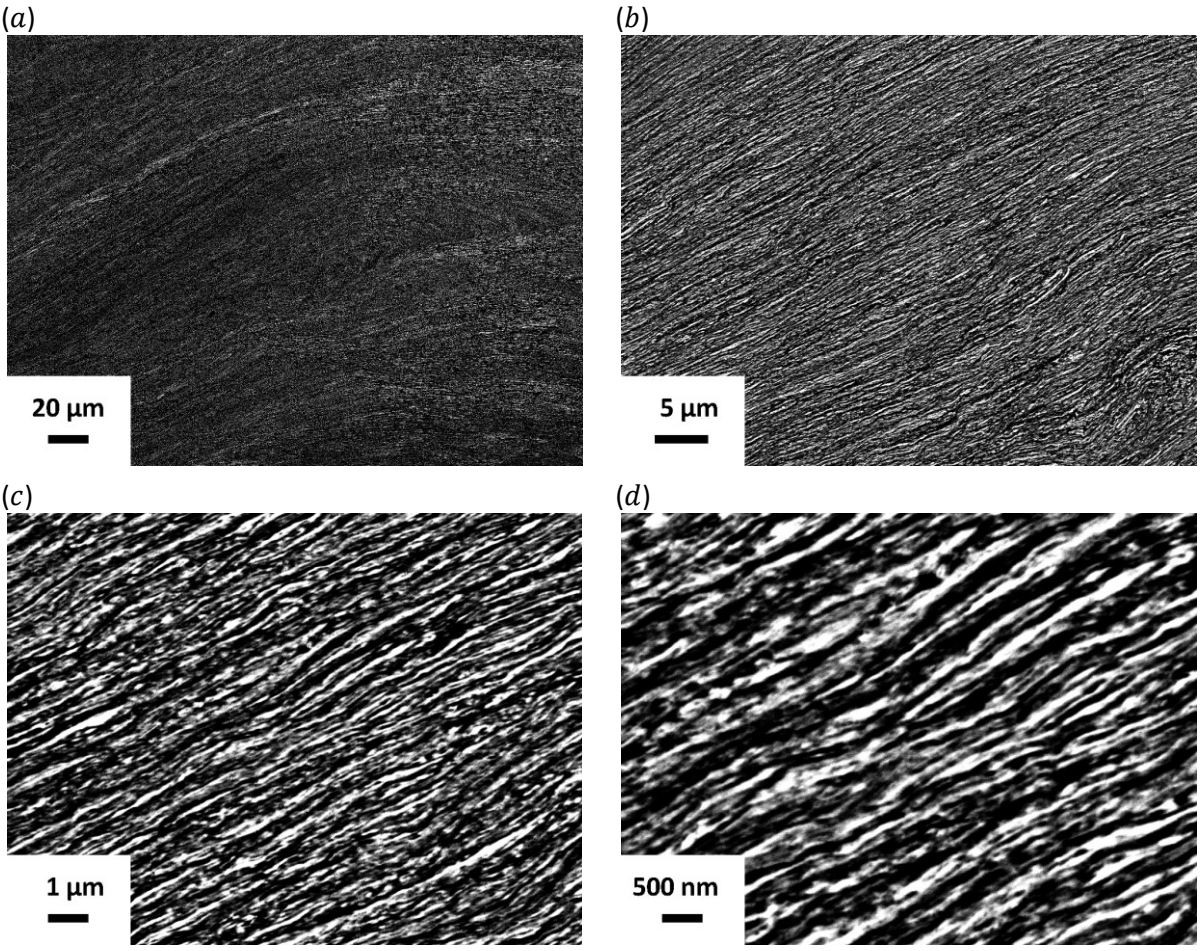

Fig. 4.6: Backscattered SEM image at R = 3.0 mm for a heat treated *two step* sample at a magnification (a) of 1,000x, (b) of 5,000x, (c) of 20,000x and (d) of 40,000x respectively.

The homogeneity of the novel Cu-Nb composite is apparent in Fig. 4.6 (a). In Fig. 4.6 (b) and Fig. 4.6 (c) the material exhibits a lamellar structure with different grain sizes. Furthermore, the deformation striations, which were observed in the LM pictures, can be examined clearly. These arise from the deformation direction of the HPT process. The nominal microstructure size of the novel Cu-Nb composite is determined to be approximately 100 nm to 200 nm in at least one direction from Fig. 4.6 (d). The length of the lamellas is not exceeding a distance of 20 µm.

Comparison of different radial position at high magnifications

Further investigations of the microstructure were carried out from a radius R_1 = 2.8 mm to a radius of R_2 = 3.6 mm in 0.2 mm steps at a magnification of 20,000x. Fig. 4.7 (a) to (d) show the structure of the composite at the respective radii. The radial position at R = 3.2 mm is not shown due to similarity to Fig. 4.7 (b) and Fig. 4.7 (c).

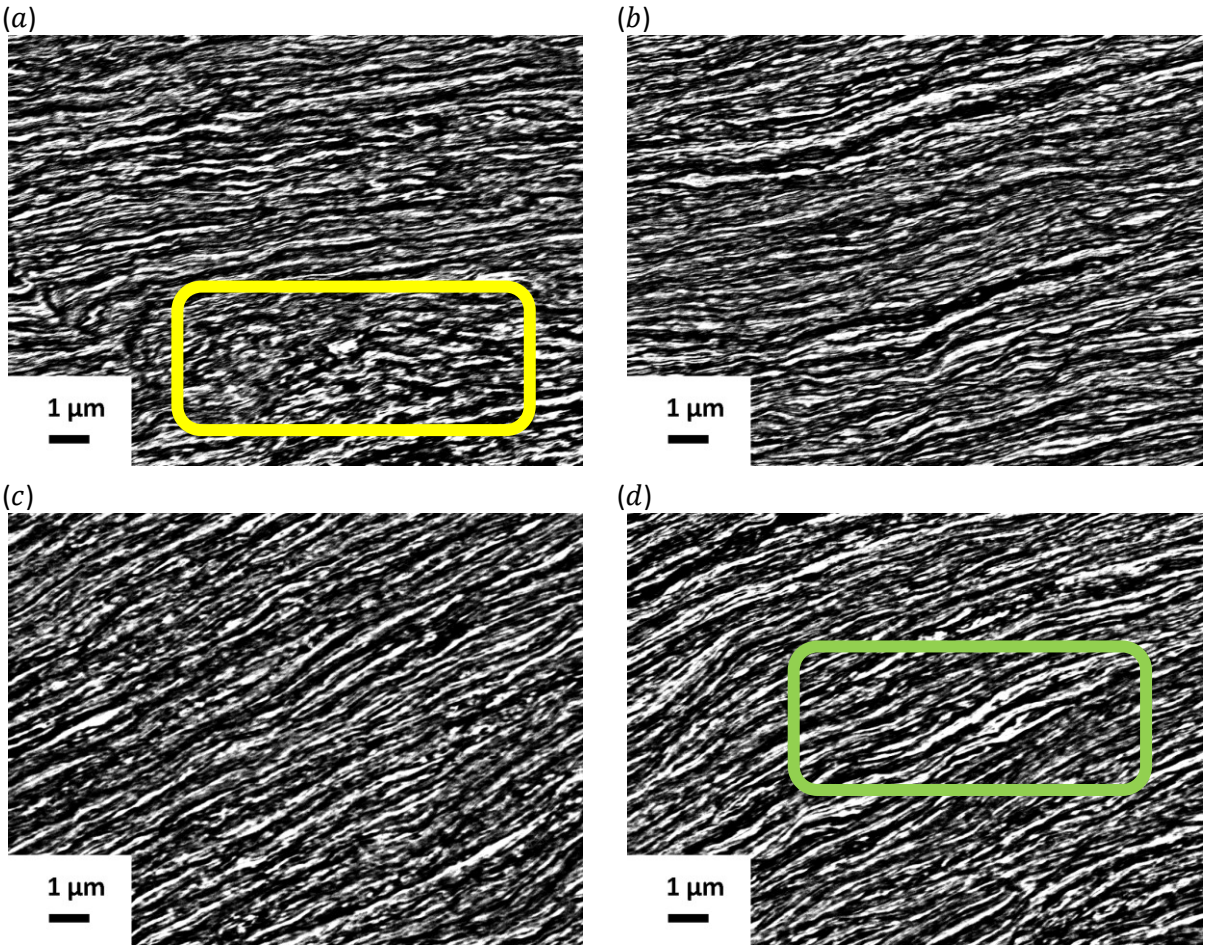

Fig. 4.7: Backscattered SEM image of the heat treated *two step* sample at (a) R = 3.6 mm, (b) R = 3.4 mm, (c) at R = 3.0 mm and (d) at R = 2.8 mm

At the outer region of the HPT sample at R = 3.6 mm, the lamellar structure started to fragment. A representative area is highlighted in the yellow rectangle in Fig. 4.7 (a). Although microhardness measurements exhibited in this area highest hardness values, it cannot be considered for further nanoindentation investigations. The disadvantage of this region is that it is not fully repeatable.

At R = 2.8 mm deformation striations with a thickness of approximately 500 nm are observed in the green rectangle in Fig. 4.7 (d). This is an indicator for lower homogeneity of the nominal structure size. With view to the discrepancy of the lamellar thickness, nanoindentation experiments should not be performed in this area.

However, besides the alignment of the deformation striations, Fig. 4.7 (b) and (c) show nearly the same microstructure over a field of around 400 µm, making these areas ideally suited for nanoindentation experiments.

Investigations after the second experimental run

After the second experimental run the temperature reference sample (Fig. 3.8) was examined in the radial position at R = 3.0 mm to verify the influence of a long time heat treatment. The investigations were performed at a magnification of 5,000x and 20,000x.

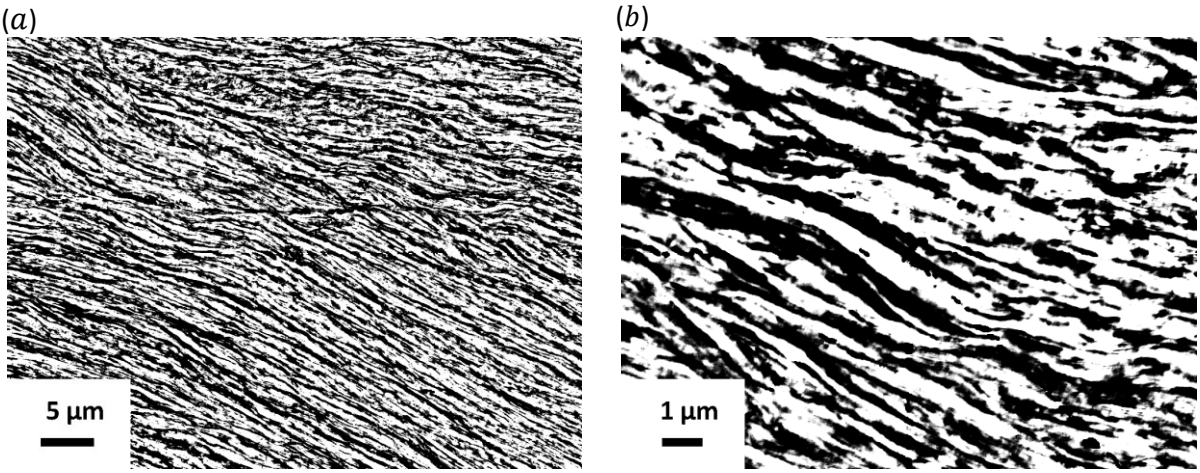

Fig. 4.8: Backscattered SEM image at R = 3.0 mm for a heat treated *two step* sample after high temperature nanoindentation at a magnification (a) of 5,000x, and (b) of 20,000x respectively.

In Fig. 4.8 (a) the influence of the exposure at higher temperatures for longer time is evident. Compared to the initial state, shown in Fig. 4.6 (b), the microstructure after the second experimental run is coarsened. Fig. 4.8 (b) indicates a significant increase of the grain size, compared to the grain size estimated to be between 100 nm and 200 nm in Fig. 4.6 (d). The grain size of the Cu-Nb composite after the experimental run is estimated to be in the range from 400 nm to 500 nm, showing a maximum lamella thickness of approximately 800 nm.

4.3 Nanoindentation hardness testing

4.3.1 Load – displacement curves

Test run at room temperature

A pre-experimental run was carried out in order to identify the optimal testing conditions for further instrumented indentation measurements. A heat treated *two step* HPT sample was mounted with super glue on a common sample holder. The area function (AF) calibration was performed on fused silica prior to the indents.

The first experiment (Fig. 4.9 (a)) was performed to evaluate the required load for an appropriate indentation depth. A depth controlled method was used (red curve in Fig. 2.2), where the minimum depth was set to 500 nm and the maximum depth to 1200 nm. The dwell period at maximum load was set to 30 seconds.

According to the received results a load of 100 mN was chosen as advisable load for further tests. This decision was made due to the fact that the AF of the indenter tip showed the best results in the range from 600 nm to 1000 nm penetration depth. A load of 100 mN results approximately in a maximum indentation depth of 800 nm and a plastic depth of 700 nm.

(a) (b)

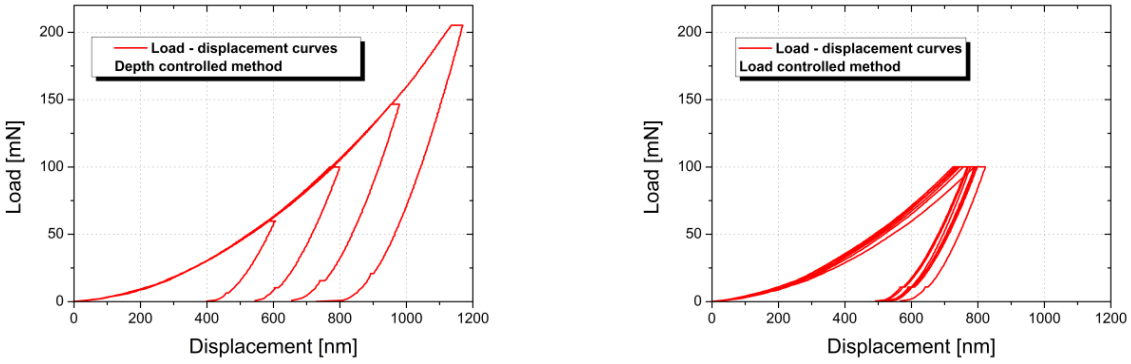

Fig. 4.9: Test indents at RT. (a) Depth controlled indents from 500 to 1200 nm maximum penetration depth. (b) Load controlled test indents with a maximum load of 100 mN.

Additional tests were performed (Fig. 4.9 (b)) with a load of 100 mN but different conditions compared to the first experiments. The major modifications were a load controlled method (black curve in Fig. 2.2) and an extended dwell time in order to achieve a relaxation behaviour (short time creep) of the material.

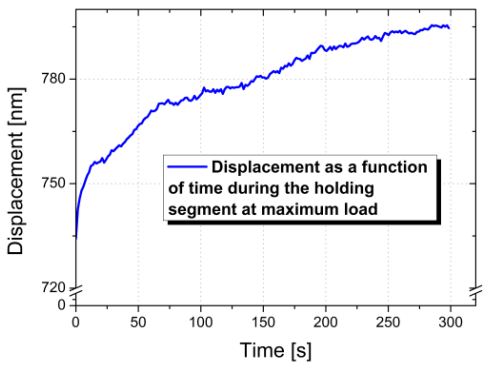

Fig. 4.10: Test run at RT showing the relaxation behaviour at maximum load over the holding segment of 300 seconds for a representative indent. The curve is used to determine the SRS.

The observed relaxation behaviour of the composite (dwell period data) is shown in Fig. 4.10 for a representative indent. According to Peykov et al. [31], it is possible to measure time-

dependent properties – such as the strain rate sensitivity (SRS) and hence the activation volume of plastic deformation (AV) – with this type of experiments. This short time creep tests were already mentioned in chapter 2.2, and will be discussed in depth later in this work.

A second method to determine time dependent properties – SRS and AV – is the constant strain rate (CSR) method. The CSR method was discussed in chapter 2.2. In Fig. 4.11 (a) and Fig. 4.11 (b) the load – displacement curves of the CSR set are shown.

(a) (b)

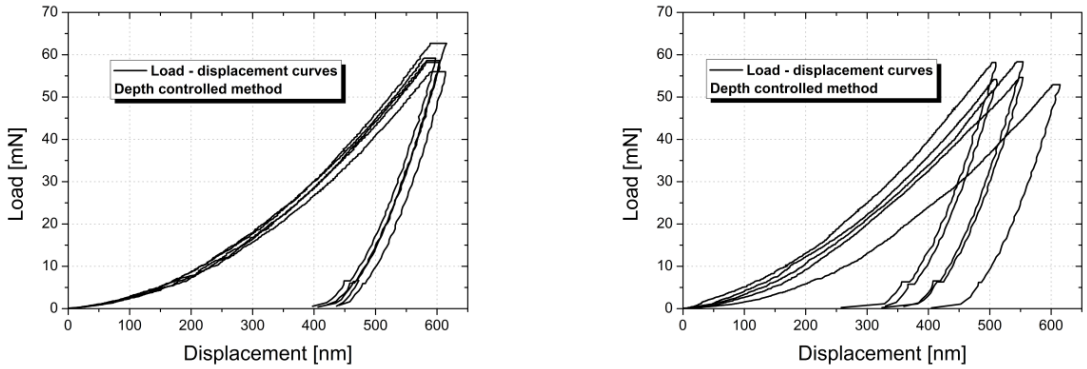

Fig. 4.11: Test run at RT showing depth controlled measurements with a proportional constant of (a) k = 0.1 and (b) k = 0.01. The curves are used to determine the SRS.

The measurements were performed in the depth controlled method with a proportional ramp type (magenta curve in Fig. 2.2). The difference between these two tests was the proportional constant, which determined the strain rate, resulting in a different load – displacement behaviour.

However, the CSR method was refused due to the apparent scatter of the load – displacement curves, especially in Fig. 4.11 (b), and hence difficult analysis of the data. The CSR method was influenced by two circumstances. First, the measurements are limited by the machine, due to the fact that fast indentation and thus high strain rates cannot be well realized. Second, very low strain rates were influenced by the noise level and vibrations.

First experimental run from room temperature to 300°C

The first experimental run was performed on a heat treated *two step* HPT sample from room temperature (RT) to an end temperature of 300°C. The temperature profile of the experimental run is shown in Fig. 3.10 (a).

In order to investigate basic mechanical properties, such as elastic modulus and hardness, as well as time dependent properties, such as strain rate sensitivity and activation volume, two different experimental sets varying in the dwell time period (load controlled method as

shown in Fig. 2.2) were carried out. The load – displacement curves are shown in Fig. 4.12 to Fig. 4.15 (black curves). These curves are used to calculate the before mentioned mechanical properties as a function of temperature, where (a) always has a dwell time of 5 seconds and (b) a 300 seconds dwell time, respectively.

The RT measurements are shown in Fig. 4.12 (a) and (b). The maximum depth is in the range of 800 nm, whereas the scattering is minimal. The load – displacement curves at 100°C show a similar shape. Due to the softening of the material slightly higher penetration depths are achieved – Fig. 4.13 (a) and (b). Particularly in Fig. 4.13 (b) a slight increase in the scatter is seen.

At 200°C the curves show increased scattering and a significantly higher penetration depth – Fig. 4.14 (a) and (b). The maximum occurring thermal drift rate is still not exceeding 0.30 nm drift per second. The measurements at 300°C exhibit even higher penetration depths as well as scattering of the particular indent curves. A difference to prior load – displacement data is the different shape of the individual indent curves, indicating a lower unloading stiffness.

After the first experimental run the indenter tip was examined under a LM. A silver shiny coating was observed. It was assumed that the indenter tip was coated with Nb, which influenced the tip geometry and consequential the AF.

Thus a new AF of the tip was calculated with the fused silica calibrating sample. The AF of the cBN indenter before the high temperature measurements and after the measurements at elevated temperatures is shown in table 4.2 (see equation 2.6).

Table 4.2: Area function parameters before and after the first experimental run.

Condition	Parameter a	Parameter b	Parameter c
Before heat treatment	20.09	24500.00	281088.76
After heat treatment	14.71	22683.20	157042.69

Furthermore, based on the change of the unloading stiffness at 200°C, as can be seen in Fig. 4.14 (a) and Fig. 4.14 (b), it was assumed that the indenter tip changed in the temperature region between 100°C and 200°C, and thus the new AF should be applied from the point, where the change in the stiffness is observed (at 200°C), when analysing the load – displacement curves. In other words: the RT and 100°C data, shown in Fig. 4.12 and Fig. 4.13, were analysed with the AF before the heat treatment; the 200°C and 300°C data from Fig. 4.14 and Fig. 4.15 with the second AF after the heat treatment.

Fig. 4.12 (a)

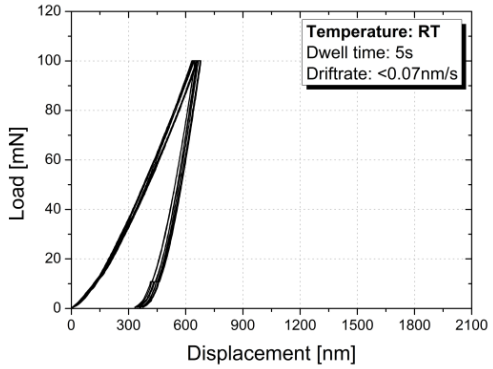

Fig. 4.12 (b)

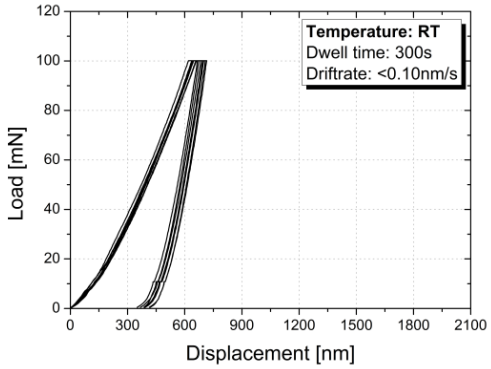

Fig. 4.13 (a)

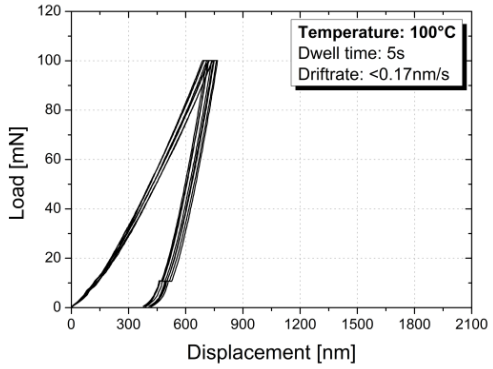

Fig. 4.13 (b)

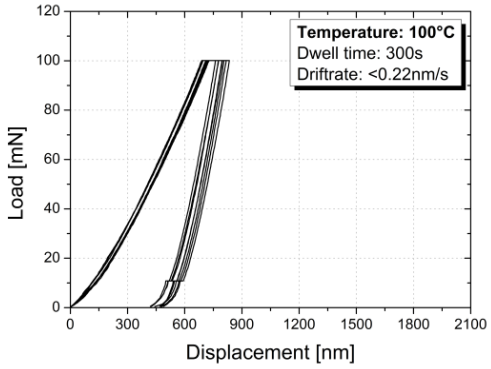

Fig. 4.14 (a)

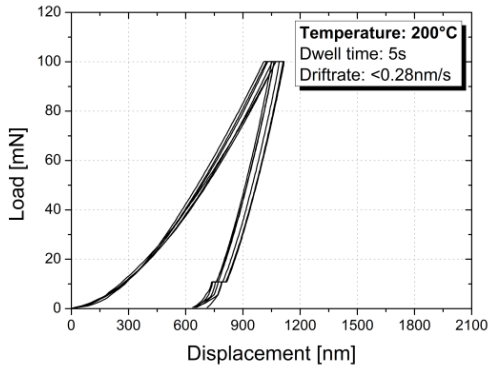

Fig. 4.14 (b)

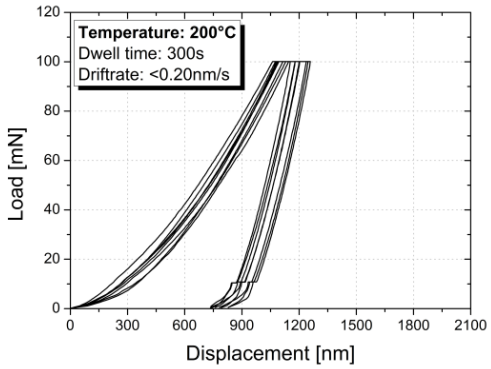

Fig. 4.15 (a)

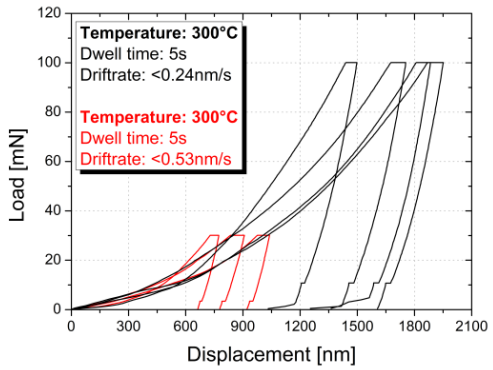

Fig. 4.15 (b)

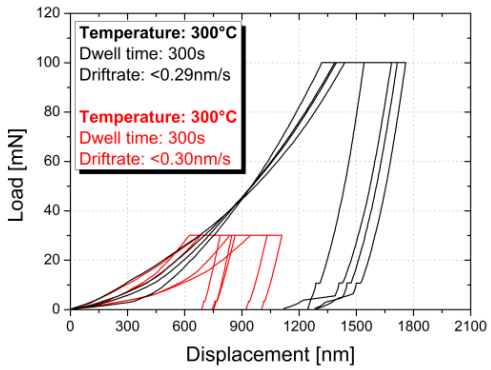

Fig. 4.16 (a)

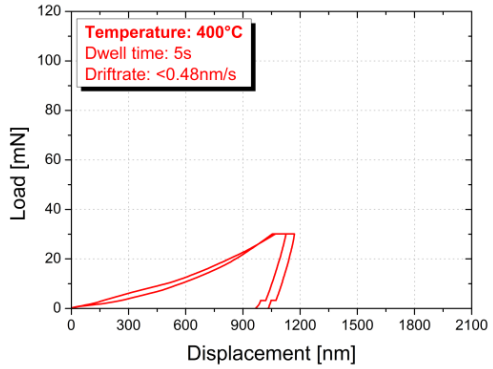

Fig. 4.16 (b)

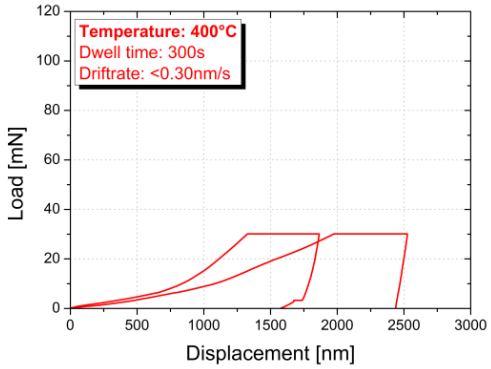

Fig. 4.17 (a)

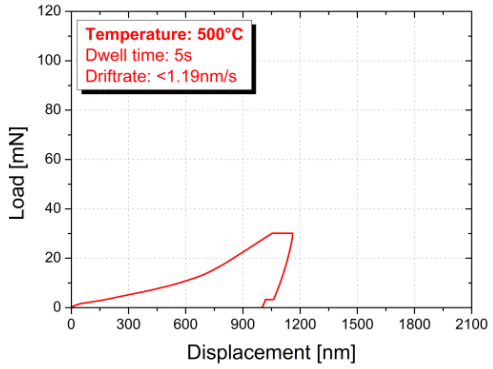

Fig. 4.17 (b)

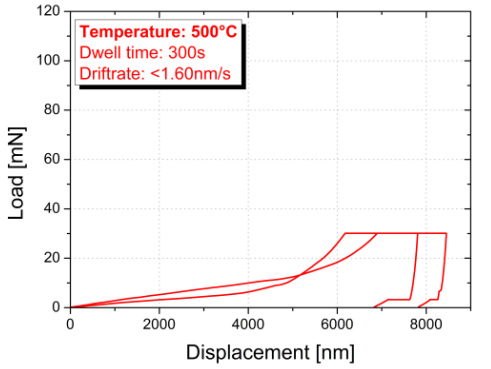

Fig. 4.12 to Fig. 4.17: Load – displacement curves of the first experimental run (black curves) and the second experimental run (red curves) with a dwell time of (a) 5 seconds and (b) 300 seconds. The testing temperature, the dwell time and the thermal drift rate are indicated in each diagram.

Second experimental run from 300°C to 500°C

The second experimental run was performed on a nominally identical heat treated *two step* HPT sample, starting at 300°C to a maximum temperature of 500°C. The temperature profile of this run can be seen in Fig. 3.10 (b).

In order to verify the data from the first experimental run, the second run started with measurements at 300°C. In this run two experimental settings with the load controlled method were carried out, whereas the maximum load was decreased to 30 mN. This change was necessary to avoid very high maximum penetration depths. The strain rate at the end of the loading segment was kept constant to 0.1, as in the first experimental run. The load – displacement curves obtained from the second experimental run are shown in Fig. 4.15 to Fig. 4.17 (red curves).

The measurements at 300°C from the second experimental run (red curves) are plotted together with the measurements at 300°C from the first experimental run (black curves) in Fig. 4.15 (a) and (b). The thermal drift was higher compared to the first run tests. The drift rate exceeds 0.50 nm per second, resulting in just a few acceptable load – displacement curves.

As in the first run, the data differed from each other in the curve shape especially at higher temperatures, indicating a change of the indenter tip geometry.

At 400°C most of the load – displacement curves exhibited strange shapes of the curves. Thus only two curves for the short and the long dwell period were appropriate for further investigations – Fig. 4.16 (a) and (b). The maximum thermal drift rate showed similar values to prior tests. Due to this fact the different curves could not be explained by drift induced errors. It was rather assumed that the high temperature cement crumbled and thus influenced the nanoindentation experiments. At 500°C the same problems occurred, resulting in high penetration depths especially in the tests with the long holding segment – Fig. 4.17 (a) and (b). Moreover, the thermal drift exceeded by far a value of 1.0 nm per second. Due to this fact the data processing and analysing of the 500°C data should be handled with care. The load – displacement curves exhibit a shape, which is not typical for indentation curves.

After the measurements at higher temperatures a new calibration of the indenter tip AF was carried out in order to verify the shape and the geometry of the cBN indenter. The same assumption was made as in the first experimental run (modification of the indenter tip during high temperature testing). Because of this assumption the load – displacement curves were analysed with the AF measured after the experiment. In table 4.3 the AF parameters for equation 2.6 are shown before and after the high temperature experiments.

Table 4.3: Area function parameters before and after the second experimental run.

Condition	Parameter a	Parameter b	Parameter c
Before heat treatment	23.66	7470.55	-40290.39
After heat treatment	15.57	13981.31	----------

It has to be noted that the frame compliance was changed from 0.305 to 0.45 to obtain a proper fitting for the fused silica values for the AF after the heat treatment. Nonetheless, a notable difference between the AF parameters before and after the heat treatment is visible, indicating a significant tip wearing during the second experimental run.

4.3.2 Young's modulus

The reduced modulus of the Cu-Nb composite as a function of temperature is shown in Fig. 4.18. The reduced modulus was calculated by equation 2.7. The unloading curve was fitted with a power law fit function starting at 100% of the maximum load and ending at 20% of the maximum load. The load – displacement curves from the first and the second experimental run with the short dwell time were used for the calculation – Fig. 4.12 (a) to 4.17 (a).

The measurements from the first run (purple curve) show a value of 107.6 ± 1.8 GPa at RT, 88.9 ± 3.2 GPa at 100°C, followed by 59.0 ± 1.8 GPa at 200°C. A decrease in the modulus from the value at RT to 47.8 ± 3.8 GPa at 300°C is obvious, indicating a drop of approximately 55%.The results obtained from the second experimental run (orange curve) show a more constant trend over temperature; nonetheless the reduced modulus exhibits a decrease too, but not as high as in the first run. The reduced modulus at 300°C is 64.3 ± 9.4 GPa and goes down to 49.1 ± 3.0 GPa at 400°C. At 500°C a modulus of 54.5 GPa is apparent, indicating a drop of approximately 15% to the first value. Notably, the data from the first experimental run is not in accordance with the outcomes from the second experimental run at 300°C.

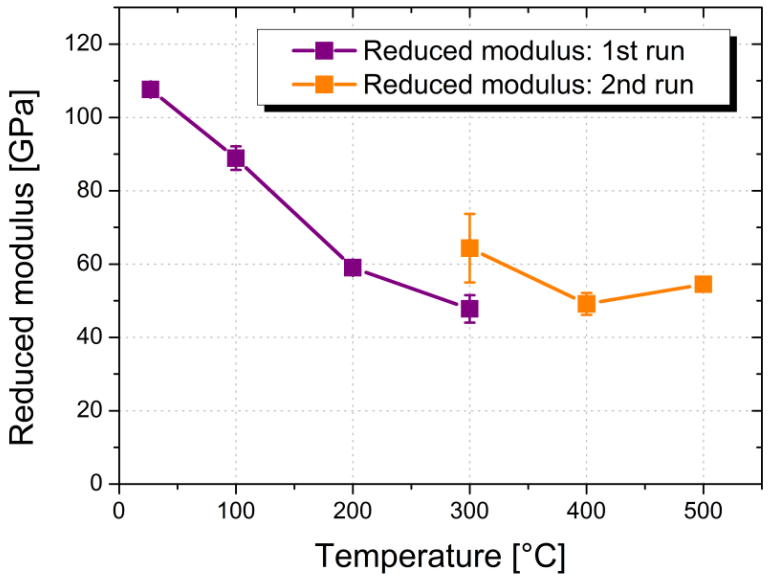

Fig. 4.18: Reduced modulus as a function of temperature obtained from the nanoindentation tests, with the results from the first experimental run (purple) and the second experimental run (orange).

In order to obtain Young's modulus values from the reduced modulus data, equation 2.8 was used and transformed to the elastic modulus of the sample (E_s). In table 4.4 the data for the calculation is shown, whereas the Poisson's ratio of the sample (ν_s) was calculated by a rule of mixture with the volume fraction of the composite. The data for the Poisson's ratio for Cu and Nb were taken from [43].

Table 4.4: Data for the calculation of the Young's modulus with a cBN indenter.

Name	Value	Unit
Young's modulus of the indenter (E_i)	800	GPa
Poisson's ratio of the indenter (ν_i)	0.12	-
Poisson's ratio of the sample (ν_s)	0.37	-

The indenter material was cubic boron nitride. The reduced modulus as a function of temperature (E_r) was taken from the experiments. In Fig. 4.19 the Young's modulus as a function of temperature can be seen together with the reduced modulus data from Fig. 4.18.

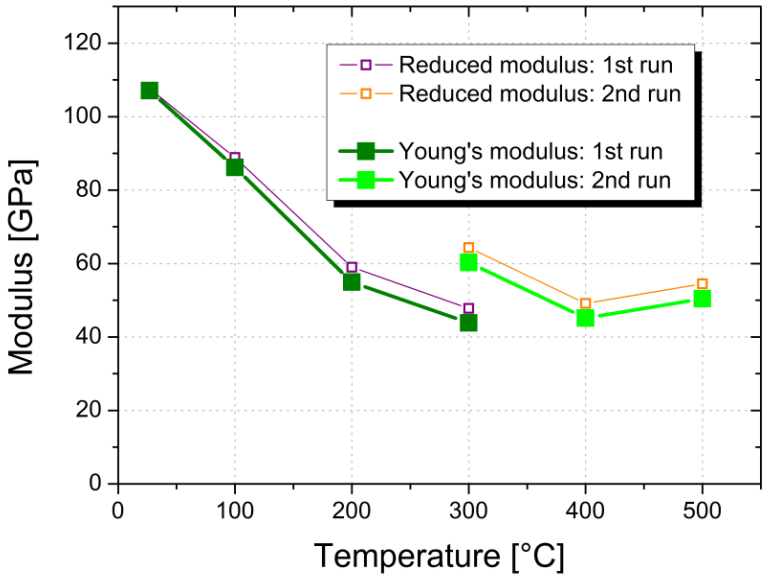

Fig. 4.19: Reduced modulus (purple and orange) as a function of temperature compared to the calculated Young's modulus (dark green and green).

The purple and magenta curves in Fig. 4.19 indicate the reduced modulus of the composite, obtained from the indentation experiments. The dark green and light green curves show the calculated Young's modulus.

The difference between these two data sets is not significant when using the Poisson's ratio and the Young's modulus of boron nitride for the indenter tip. The difference is in the range from 5% to 10%.

4.3.3 Hardness

The hardness of the Cu-Nb composite as a function of temperature obtained from the nanoindentation experiments is shown in Fig. 4.20. In order to assess the hardness values the load – displacement curves with the short dwell time at maximum load were used to avoid any kind of relaxation of the material – Fig. 4.12 (*a*) to Fig. 4.17 (*a*). The hardness values were calculated with equation 2.3.

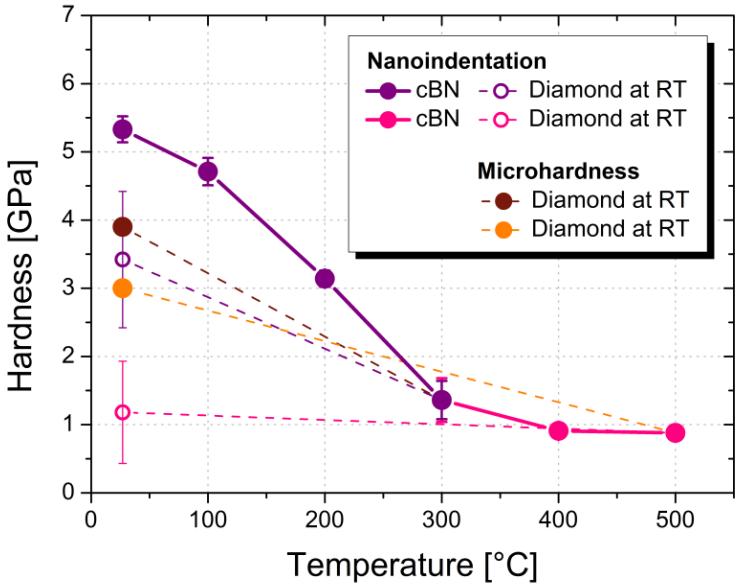

Fig. 4.20: Hardness as a function of temperature obtained from the first experimental run (purple) and the second experimental run (orange). The hardness was also measured again at RT for the different experimental runs after the high temperature experiments.

The purple curve shows the results from the first experimental run from RT to 300°C, the orange curve represents the outcomes of the measurements from 300°C to 500°C. Different than the modulus data, the hardness values from the first run at 300°C are in accordance with those from the second run at 300°C.

At RT the hardness of the Cu-Nb composite is 5.33 ± 0.19 GPa. A slight decrease of around 12% to 4.71 ± 0.20 GPa at 100°C is obvious. The hardness values at 200°C are 3.14 ± 0.12 GPa and 1.36 ± 0.28 GPa at 300°C, respectively. A significant overall decrease of more than 75% is apparent.

The hardness from the second run shows a more constant trend, but also a lower level compared to the values from the first experimental run. The hardness at 300°C is 1.36 ± 0.32 GPa and drops to 0.91 ± 0.05 GPa and 0.88 GPa at 500°C, respectively. It has to be kept in mind that the hardness values at 400°C and 500°C were determined with a low number of load – displacement curves.

After the nanoindentation testing at elevated temperatures the hardness was measured back at RT with a diamond indenter tip (as mentioned in chapter 3.6.1). The hardness at RT after the first experimental run was determined to be 3.42 ± 1.00 GPa, indicating a change to the starting sample hardness of approximately 36%. After the second experimental run a hardness value comparable to the hardness at 300°C, namely 1.18 ± 0.75 GPa, was observed.

In order to avoid the influence of the oxide layer on the results, the hardness of the testing reference sample (Fig. 3.8) was investigated by microhardness measurements (Fig. 4.20). The samples were embedded and polished with the same procedure as described in 3.4.2. On the one hand the hardness after the first experimental run showed a value of approximately 3.9 GPa, assuming a minor influence of the oxide. On the other hand, in the case of the second experimental run, the hardness value was higher compared to the nanoindentation results, exhibiting 3.0 GPa. These findings indicate an influence of the oxide layer especially in the second experimental run.

4.3.4 Strain rate sensitivity

Analysing methods

The strain rate sensitivity (SRS) was determined by the constant load (CL) method according to [31]. The calculation was carried out in a Microsoft Office 2007 Excel sheet, while the fitting was realised in OriginPro 8. A description of the method and the equations used was provided in chapter 2.2 of this work. The two most important parameters for calculating the SRS are the natural logarithm of the hardness and of the strain rate as a function of time.

In the following, the procedure will be described with a representative single indent. For the analysis of the SRS the dwell period curves of the load – displacement curves with the long dwell time at maximum load were used. In Fig. 4.21 the dwell curve is shown.

In order to calculate the strain rate ($\dot{\varepsilon}$) from the displacement (h), the first derivative is required. Therefore, the relaxation curve was fitted with a power law function (equation 4.1).

$$y = A * |x - x_c|^P \qquad \text{(Eq. 4.1)}$$

(a) (b)

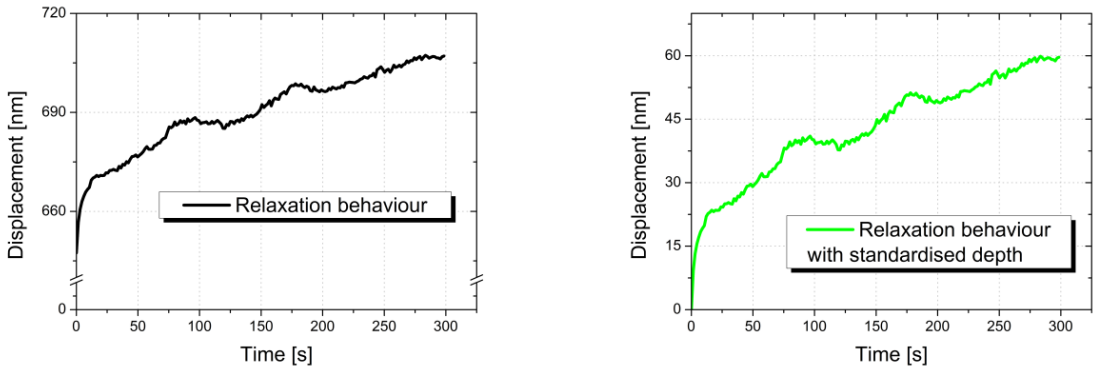

Fig. 4.21: (a) Relaxation curve obtained from the holding segment at maximum load from the constant load measurements and (b) standardised relaxation curve.

To do so, the first step was to subtract the displacement at the beginning of the holding segment (h_0) from all data points in Fig 4.21 (a). The resultant curve, Fig. 4.21 (b), is similar to the curve obtained from the measurements, Fig. 4.21 (a), but the displacement h on the ordinate is replaced by the standardised displacement h-h_0. This step was necessary in order to be able to fit the displacement curve with the power law fit function.

In a second step, the curve in Fig. 4.21 (b) was fitted with the above mentioned power law fit function. The received fit function (red curve) as well as the standardised displacement (green curve) data is shown in Fig. 4.22. Three parameters (x_c, A and P) were obtained from the Origin software as fitting parameters.

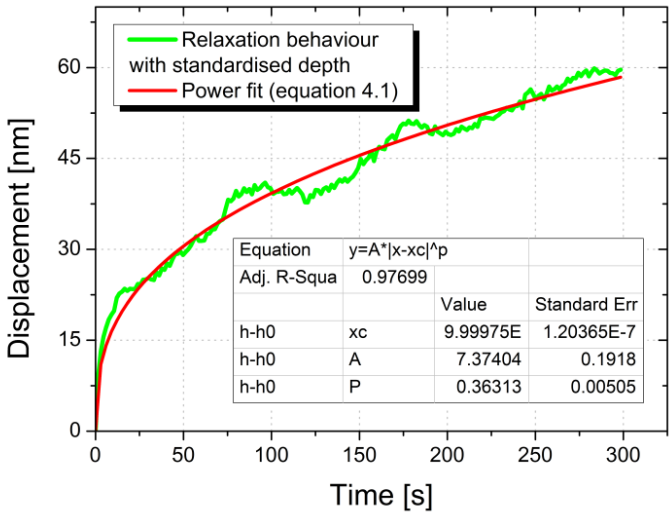

Fig. 4.22: Power law fit (red curve) of standardised relaxation curve (green).

According to Peykov et al. [31] the displacement curve can be divided into two stages. These two stages were named S*tage a* and *Stage b*, whereas *Stage a* ranges from the beginning of the holding segment to 20 seconds. The *Stage b* ranges from half of the duration time to the end of the holding segment.[2] Furthermore, Peykov et al. described that the results obtained from *Stage a* are in better agreement with SRS results from different analysing methods than results from *Stage b*. The *Stage b* results show approximately ten times higher values. Despite this fact the SRS of both stages was determined with the CL experiments, but with more attention to *Stage a*.

The following steps will be described only for *Stage a* due to the similarity of the analysis for both steps. After fitting the standardised displacement curve with the fit function, as shown in Fig. 4.23 (a), the displacement at the beginning of the holding segment (h_0) was added again to all the data points.

[2] Explanatory notes: Short time creep tests described in this work should not be confused with standard creep tests. For this reason, the stages were not specified as S*tage I* and *Stage II*, as used in creep tests and in [31].

(a) (b)

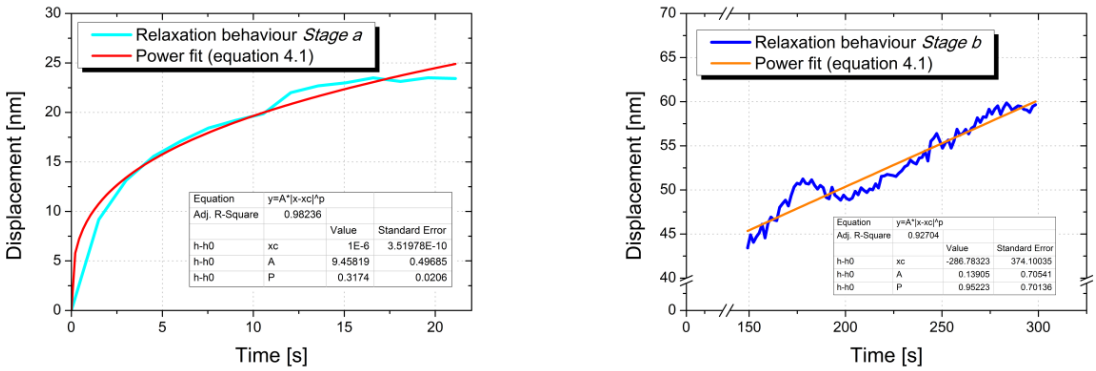

Fig. 4.23: Power law fit of (a) *Stage a* and (b) *Stage b*.

This step is important due to the fact that the strain rate is calculated by dividing the first derivative of the displacement by the displacement itself (h) and not by the standardised displacement (h-h_0). By dividing the first derivative of the displacement by the displacement, the strain rate as a function of time $\dot{\varepsilon}(t)$ can be received. Hence, the natural logarithm of the strain rate as a function of time – ln $\dot{\varepsilon}(t)$ – can be achieved. The hardness as a function of time $H(t)$ and thus the natural logarithm of the hardness over time – ln $H(t)$ – were calculated by dividing the maximal load (P_{max}) by the contact area (A_c) at a specific testing time. Finally, the strain rate sensitivity is the slope of the data when plotting on the ordinate the time dependent natural logarithmic hardness and on the abscissa the time dependent natural logarithmic strain rate.

This representative indent has for *Stage a* a slope (light grey linear fit) and hence a strain rate sensitivity of 0.020. For *Stage b* the slope (dark grey linear fit) and thus the m-value is 0.073 (Fig. 4.24).

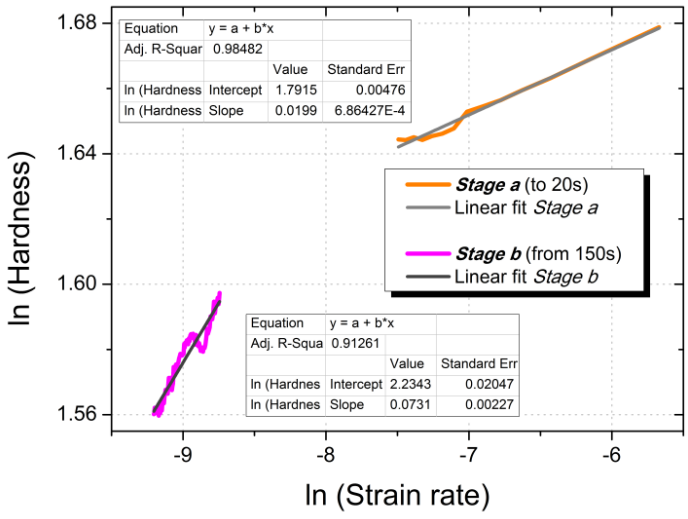

Fig. 4.24: Double logarithmic curve used for calculation of the SRS through linear fitting curves. *Stage a* (orange curve) and *Stage b* (magenta curve) are fitted by two different fit functions.

In the Fig. 4.25 (a) to (f) the double logarithmic curves (natural logarithm of the hardness over the natural logarithm of the strain rate) are shown for each temperature. The testing temperature and the obtained SRS for the two stages are indicated.

The SRS values were calculated with equation 2.9 using the load – displacement curves with the long dwell time, Fig. 4.12 (b) to 4.17 (b), whereas the orange curves represent *Stage a* and the magenta curves represent *Stage b*.

Fig. 4.25 (a)

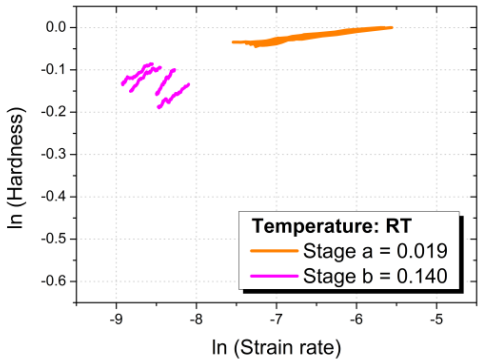

Fig. 4.25 (b)

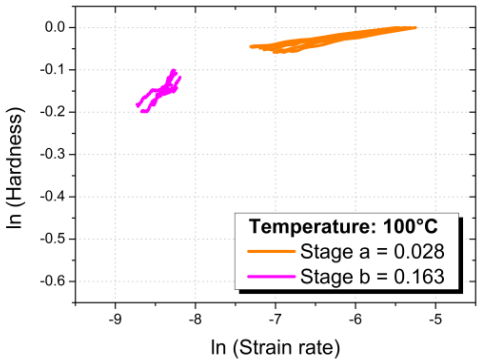

Fig. 4.25 (c)

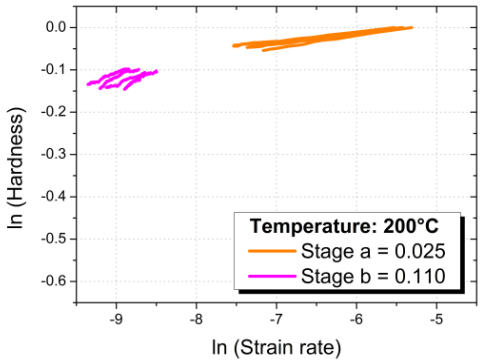

Fig. 4.25 (d)

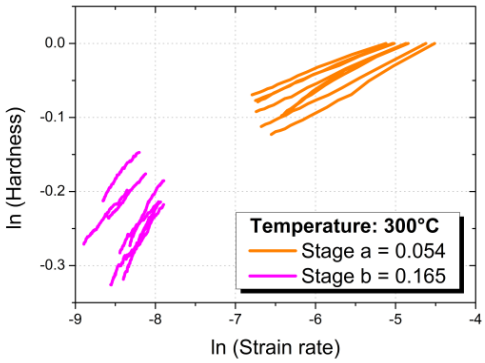

Fig. 4.25 (e)

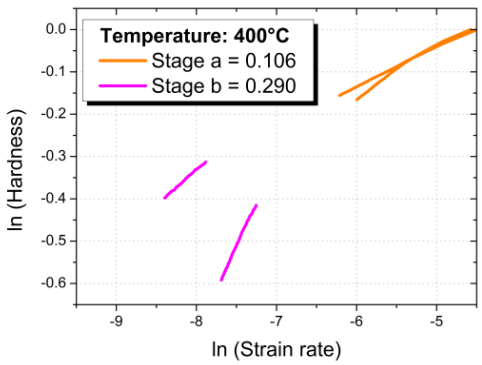

Fig. 4.25 (f)

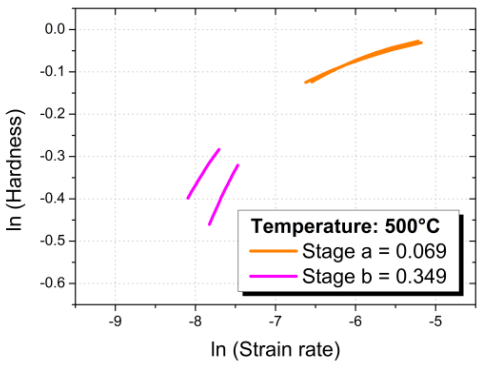

Fig. 4.25: Strain rate sensitivity data in a double logarithmic plot showing *Stage a* (orange) and *Stage b* (magenta) for (a) RT, (b) 100°C, (c) 200°C, (d) 300°C, (e) 400°C and (f) 500°C.

Fig. 4.26 shows the strain rate sensitivity values obtained from *Stage a* and *Stage b*. The difference between these two stages is obvious. The SRS values of *Stage b* exhibit at elevated temperatures (400°C and 500°C) values in the range of 0.30.

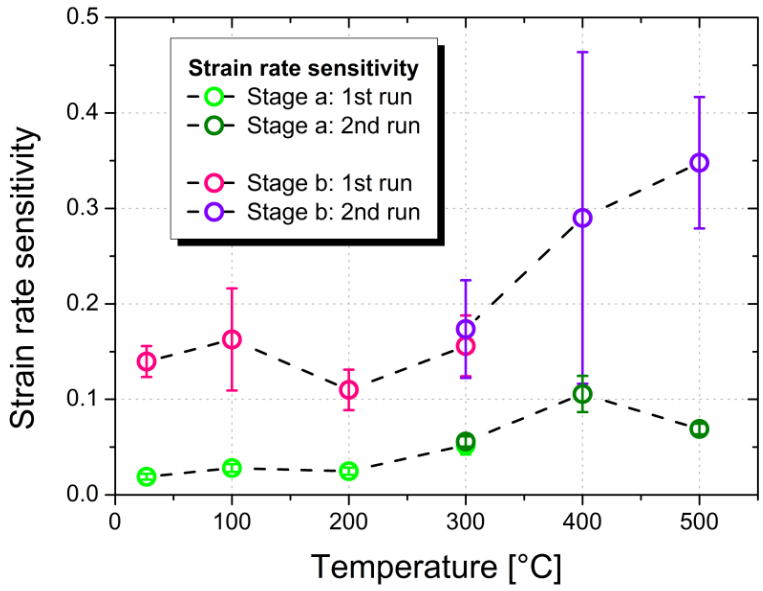

Fig. 4.26: Strain rate sensitivity as a function of temperature showing *Stage a* and *Stage b*.

These values seem to be overestimated, due to the fact that at this temperatures (homologous temperature of approximately 0.5 in the case of Cu; smaller than 0.3 in the case of Nb) no diffusion process should occur. For this reason, the values obtained from *Stage b* should not be further investigated.

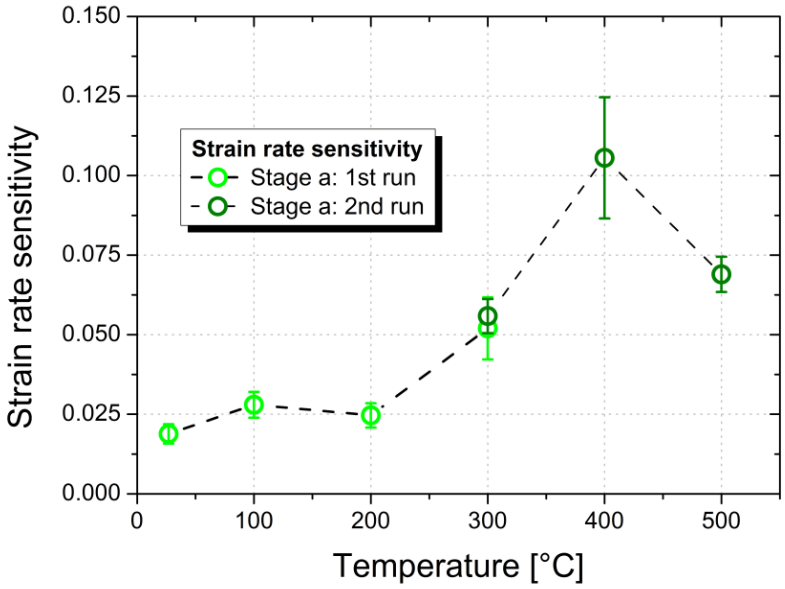

Fig. 4.27: Strain rate sensitivity as a function of temperature showing *Stage a*.

In Fig. 4.27 the strain rate sensitivity values for *Stage a* are shown. At the first testing temperatures (RT to 200°C) the Cu-Nb composite exhibits lower SRS in the range of approximately 0.020. The values are lower than at elevated temperatures (above 300°C). At RT the observed SRS is 0.019, at 100°C 0.028 and at 200°C 0.025 respectively.

An increase of the SRS from approximately 0.020 to 0.052 is apparent in the range between 200°C and 300°C. This value gets even higher at 400°C reaching 0.106, followed by a drop to 0.069 at the maximum testing temperature of 500°C. An overlapping of the values from the first and the second experimental run at 300°C is obvious (strain rate sensitivity for the first experimental run is 0.052, for the second experimental run 0.056).

4.3.5 Activation volume

In order to determine the governing deformation mechanism of the Cu-Nb composite at each temperature, the activation volume was calculated using equation 2.11 and equation 2.12. A logarithmic diagram of the activation volume as a function of testing temperature can be seen in Fig. 4.28 for two different analysing methods. The Burger's vector (b) was set to b = 0.28 nm according to a rule of mixture calculation by Zhu et al. [44].

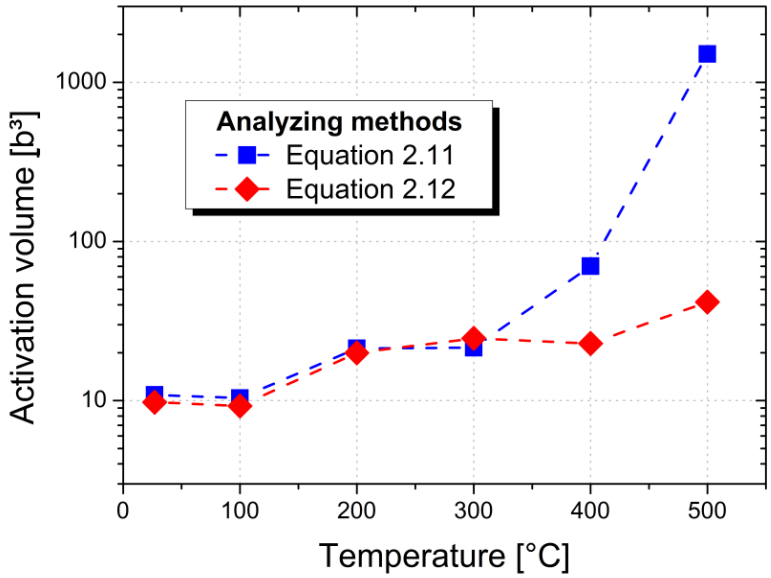

Fig. 4.28: Activation volume for a Burger's vector of b = 0.28 nm analyzed by two different methods.

The two different analysing methods show an impressive overlap to a temperature of 300°C. The activation volume ranges from 10 b^3 at RT and 100°C, to 20 b^3 at 200°C and 24 b^3 at 300°C indicating a slight increase over temperature. In the case of the first analysing method (equation 2.11) the activation volume shows at 400°C approximately three times higher values, 70 b^3, than at prior temperatures. At 500°C the value rises again more than 15 times

higher compared to prior temperatures to approximately 1510 b^3 (blue curve). In the case of the second method (equation 2.12) the activation volume shows a nearly linear trend to the maximum testing temperature. At 400°C there is no significant change, the value is 22 b^3, whereas at 500°C an increase to 42 b^3 is apparent (red curve).

5 Discussion

5.1 Microindentation testing

Higher hardness values are obtained for the samples which were prepared by a high number of revolutions, as a consequence of equation 2.2. In literature, for example [14, 15], a higher number of revolutions results in a finer microstructure and hence higher hardness values.

Furthermore, as a second consequence of equation 2.2, a gradient in the hardness is observed along the radial direction for both processing routes (*one step* and *two step* HPT), showing higher hardness values at outer regions compared to the centre of the sample [15].

The *two step* HPT process exhibited higher hardness values compared to the *one step* HPT process with low and high number of revolutions as proposed by [17]. The *one step* HPT sample with 150 revolutions had scattered microhardness values over the radial direction due to cracks.

A significant influence of the short time annealing was not observed. The *two step* HPT sample exhibited after the heat treatment nearly the same microhardness values (Fig. 4.2).

5.2 Microstructural characterisation

The characterisation of the microstructure by light microscopy (LM) confirmed the results obtained by microhardness measurements. A difference between the different processing routes is obvious (Fig. 4.4). The microstructure of the *one step* HPT sample (60 revs) could be resolved by LM, indicating a coarse grained composite, see Fig. 4.4 (a). With increasing the number of revolutions – Fig. 4.4 (b), or using the *two step* HPT deformation – Fig. 4.4 (c), the microstructure was not resolvable in the LM anymore.

Further investigations were carried out on a heat treated *two step* HPT sample using scanning electron microscopy (SEM) to examine the microstructure of the composite more in detail and to estimate the grain size of the novel Cu-Nb composite. The nominal microstructure size of the Cu-Nb composite is in the order of 100 to 200 nm in one dimension, therefore the composite has an ufg microstructure.

An area of approximately 400 µm at R = 3.0 mm shows nearly constant microhardness values and a homogeneous microstructure determined by LM and SEM.

5.3 Nanoindentation testing

5.3.1 Mechanical behaviour of the composite

Elastic modulus

In the literature the Young's modulus of a Cu-Nb composite has not been discussed yet. In order to compare and explain the results, a composite Young's modulus has been calculated with data from Cu and Nb (Fig. 2.7). The calculated Cu-Nb elastic modulus as a function of temperature (violet curve) was compared with the results from the high temperature nanoindentation testing (dark green and green curve) shown in Fig. 5.1.

According to this calculation the Young's modulus of the composite should be higher, especially at elevated temperatures, compared to what was obtained from the nanoindentation experiments in the first and the second experimental run, as can be seen in Fig. 5.1.

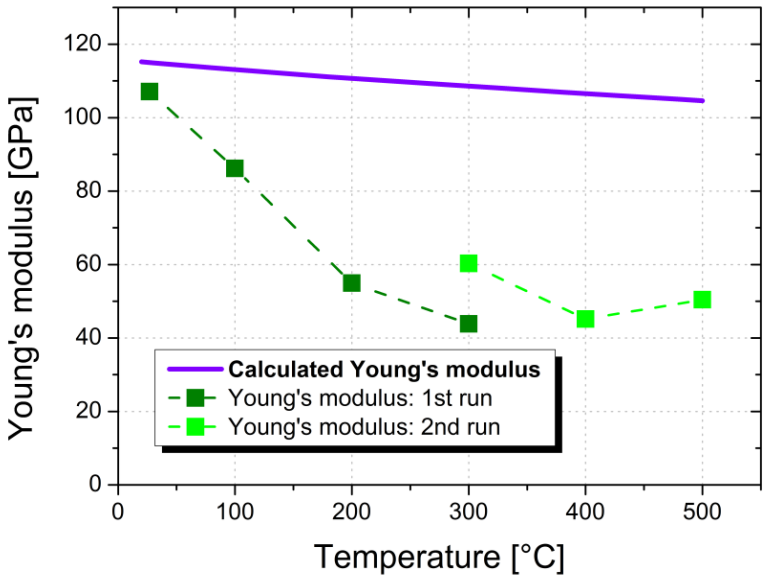

Fig. 5.1: Comparison of the calculated Young's modulus (violet) from [33] and Young's modulus obtained from first (dark green) and second (green) experimental run.

A possible explanation for this phenomenon is that the indenter material has changed and hence falsified frame compliance is achieved. This is supported by the fact that after the indentation testing at elevated temperatures the indenter tip was covered with a silver shining film. It was assumed that the indenter tip was contaminated with Nb, since Cu shines in an orange colour. Furthermore, based on the change in stiffness values during unloading, it is assumed that the contamination only occurs above 100°C.

To compensate these circumstances, the indenter tip material was changed for the analysis to Nb instead of cubic boron nitride (cBN). Equation 2.5 was used to calculate the Young's modulus with a different indenter tip material. In table 5.1 the data for the calculation is shown, taken from [43].

Table 5.1: Data for the calculation of the Young's modulus with a *"Nb" indenter*.

Name	Value	Unit
Young's modulus of the indenter (E_i)	105	GPa
Poisson's ratio of the indenter (ν_i)	0.40	-
Poisson's ratio of the sample (ν_s)	0.37	-

In Fig. 5.2 the original Young's modulus values from the first experimental run at RT and 100°C, which were analysed with the cBN indenter, are shown together with the new calculated values at 200°C and 300°C from the first run (blue), and the values at 300°C, 400°C, and 500°C (cyan) from the second run with the *"Nb" indenter*. A linear fit function was applied through these points in order to obtain a fitted curve (dark cyan curve).

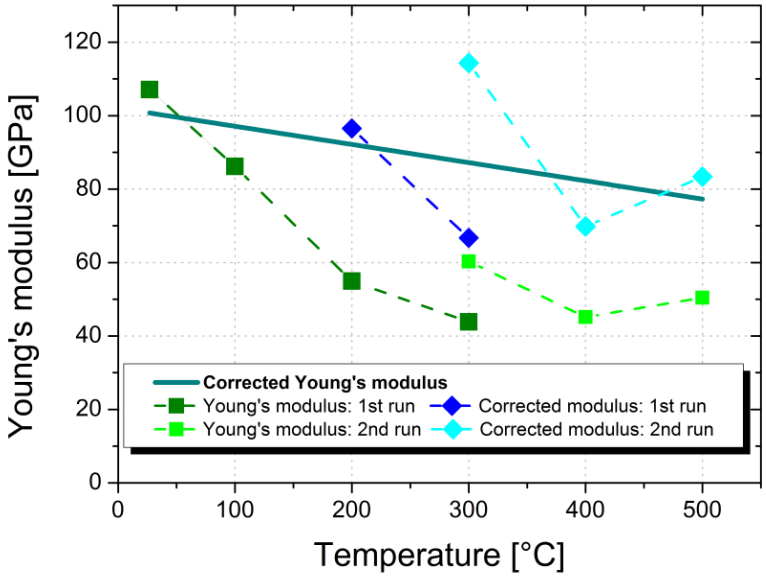

Fig. 5.2: Corrected Young's modulus data (dark cyan) obtained from measurements (dark green) and calculated values (blue and cyan) with a changed indenter tip material: from cBN to Nb.

The corrected Young's modulus data as a function of temperature (dark cyan) is compared to the calculated Young's modulus data of the Cu-Nb composite (violet). As can be seen in Fig. 5.3, the temperature dependent trend of the values is nearly the same; the values deviate only about 20% from the calculated Cu-Nb composite.

A few assumptions had to be made when analysing the elastic modulus. The obtained values from the measurements were corrected by recalculating the elastic modulus with a different massive indenter tip material, while only a thin metal layer was observed experimentally on the tip. Nonetheless, the corrected Young's modulus data of the Cu-Nb composite shows a comparable trend to the calculated Young's modulus.

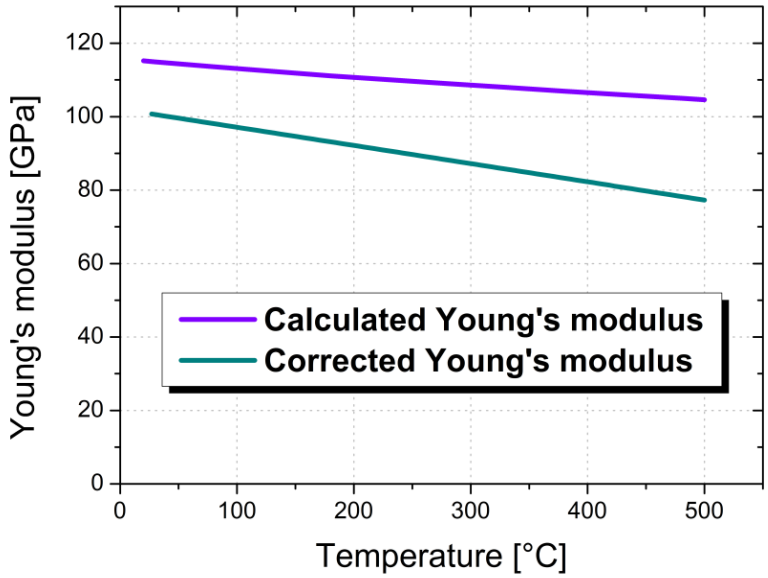

Fig. 5.3: Comparison of the calculated (violet) and corrected (dark cyan) Young's modulus.

It has to be mentioned that the mounting of the sample with the high temperature cement could have an influence on measuring the Young's modulus as well, especially at higher temperatures. As described in chapter 3.6.2, to ensure planarity a small amount of cement has to be placed under the tested sample. Due to instability of the cement, smaller values for the modulus in a temperature region between 200°C and 500°C could be obtained. Moreover, the Young's modulus of nc and ufg materials is reported to be lower compared to cg materials. This is related to the increased volume fraction of the grain boundary phase in nanostructured materials.

Comparative RT measurements were performed using an Agilent G200 facility at the Department WW1, Friedrich-Alexander University (FAU) in Erlangen-Nürnberg by Dr. Verena Maier. These tests were carried out in order to verify the results obtained from the Micro Materials facility. A constant stiffness method (CSM) and a displacement of 2000 nm were used. The Young's modulus shows a value of 129.0 ± 2.2 GPa, whereas the reduced modulus is slightly lower with 127.7 ± 2.0 GPa. The strain rate was set to 0.05 s^{-1}. The difference of these measurements compared to the results from this work can be related to the accuracy of Young's modulus measurements, which is in the range of several GPa.

Hardness

The Cu-Nb composite processed via HPT investigated in this work possesses the highest hardness of ~ 5.4 GPa at RT of all comparable materials in the ufg range at approximately 100 nm as can be seen in Fig. 5.4. Similar hardness values are only observed for nc multilayered composites with a ten time smaller structure size.[3]

One of the highest contributions to hardness of the investigated composite is attributed to the grain refinement during HPT deformation [14-17]. Furthermore, the interface between the fcc Cu and the bcc Nb acts as a barrier to the dislocation movement due to the different crystallographic system of these two elements [9]. Because of this, dislocations cannot overcome these phase boundaries in the lower temperature region (homologous temperature smaller than 0.3). A third contribution to the hardness compared to other materials can be related to the intermixing from HPT deformation of Cu in Nb grains and vice versa [17, 42].

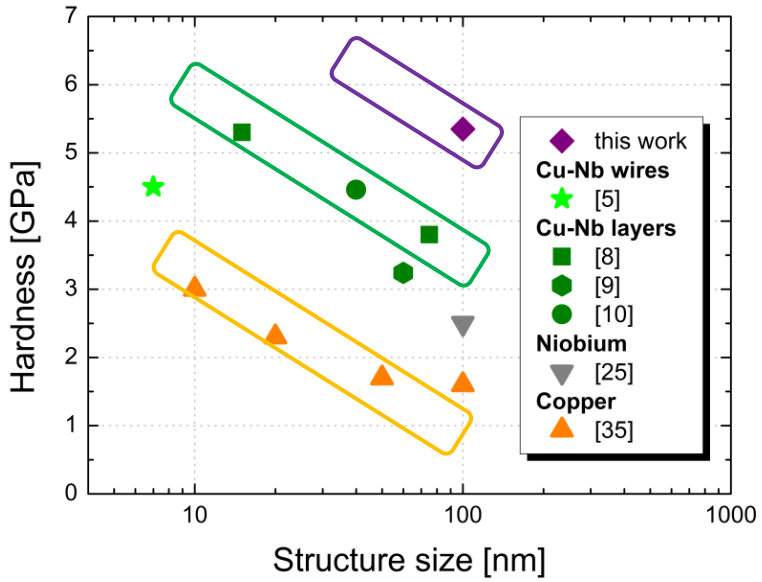

Fig. 5.4: Comparison of RT hardness values from different previous works for pure Cu, pure Nb and Cu-Nb composites. Hall-Petch scaling law indicated in coloured frames and extended by results obtained in this work (purple).

It was discussed in chapter 2.3.2 that a scaling relationship is apparent. When assuming a Hall-Petch law for the Cu-Nb HPT composite, the hardness for a structure size of approximately 10 nm can reach hardness values exceeding 7.5 GPa, as it is indicated in Fig. 5.4, which approaches the theoretical strength limit of Cu. Comparative measurements of the hardness were performed in Erlangen-Nürnberg at the FAU by Dr. Verena Maier and exhibited 5.46 ± 0.26 GPa at RT. These measurements are in good agreement with the observed values from the Micro Materials facility.

[3] Explanatory notes: Figure 2.8 was enhanced with the hardness values investigated in this work.

The hardness as a function of temperature was shown in Fig. 4.20. The hardness values from the first experimental run (purple curve in Fig. 4.20) at RT and 100°C show a nearly constant trend. A decrease of the hardness from 100°C to 200°C is apparent and can be related to thermally activated processes and softening of the material over temperature [34].

A significant drop in the range from 200°C to 300°C in the first experimental run (purple curve) is obvious. The measurements that were performed back at RT after the heating experiments (microindentation and nanoindentation) show significantly lower hardness values than the starting measurements at RT. These facts are an indication for a change in the microstructure of the *two step* HPT composite. A possible explanation for the softening is coarsening of one of the two phases, presumably the softer material Cu. As was shown in Fig. 2.9, the maximum temperature for nc and ufg Cu is approximately at 300°C, above this temperature grain growth occurs and the material softens [37].

Furthermore, the decrease of the hardness can be related to a rough, blue shining oxidation layer on the surface, which is apparent after the heating experiments. Although an Ar atmosphere was used during the experiments at higher temperatures, oxidation cannot be avoided. The thickness of the oxide layer is assumed to be in the range of 100 nm to 200 nm. The load – displacement curves from these measurements showed a significant lower Young's modulus indicating an elastic behaviour of the tested material. A possible explanation is that the oxide on the surface was elastically deformed during the nanoindentation testing and hence lower hardness values were observed.

The hardness from the second experimental run (orange curve in Fig. 4.20) shows at higher temperatures (400°C and 500°C) nearly the same values, indicating a plateau of the hardness. The measurements that were performed after the heating back at RT show lower hardness values compared to the results at RT (from the first experimental run) and at 300°C. The decrease of the values cannot be completely related to ongoing coarsening of the microstructure. This arises due to the fact that a huge difference of approximately 2 GPa between the microhardness (3.0 GPa) and the nanohardness (1.0 GPa) measurements was observed, indicating a significant influence of the oxide layer on the results. Nonetheless, the grain size of the composite has doubled compared to the initial state and exhibits even thicker lamellas of approximately 800 nm thickness.

Another contribution for the softening should be accounted. The diffusion path according to Einstein [34] was calculated for Nb as soluble in a Cu matrix to be in the range of approximately 5 nm to 10 nm at high temperatures (500°C) and long duration (5 hours). Other diffusion paths (Cu soluble in Nb matrix or lower temperatures) exhibited values less than 1.0 nm and are therefore negligible. With the observations in [17, 42] and the calculation of the dif-

fusion path, it is assumed that the Nb at the grain boundaries in the Cu grains can diffuse and hence the contribution to hardness by intermixing disappears. A contribution to the observed softening of the material can be related to this phenomenon.

The thermal stability of Cu-Nb composites was discussed in chapter 2.3.2 for cold drawn wires and multilayered composites. Both composites from Fig. 2.10 exhibit a high stability after annealing at high temperatures. The wires were heat treated for 60 minutes under an argon (Ar) atmosphere [7] and in the case of the multilayered composite an annealing for 30 minutes was carried out [8]. A hardness testing at elevated temperatures was only reported for Cu-Nb multilayered composites with a microstructure size (layer thickness) of 60 nm [9].

In Fig. 5.5 (a) the microhardness values for prior investigated Cu-Nb materials are shown together with the microhardness results obtained from this work that were performed on a *two step* HPT composite after annealing at 500°C for 60 minutes (Fig. 4.2). In Fig. 5.5 (b) the hardness measured by nanoindentation at elevated temperatures is shown for the composite investigated in this work Fig. 4.20.

(a) (b)

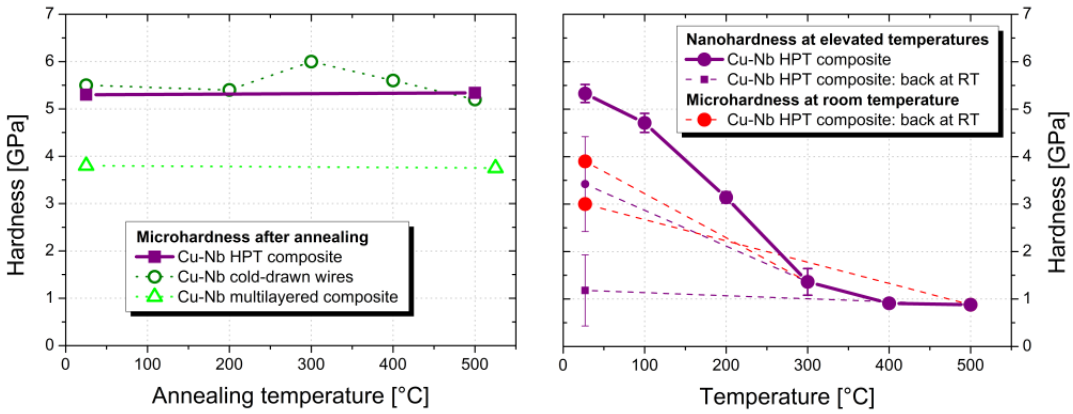

Fig. 5.5: Investigated thermal stability through (a) microhardness test subsquently after an annealing at a certain temperature and (b) nanohardness measurements at elevated temperatures.

Fig. 5.5 (a) summarizes the thermal behaviour of the investigated composite showing no influence of a short time annealing at 500°C for 60 minutes. Fig. 5.5 (b) shows the decrease of the hardness and coarsening of the composite in-situ during long time heat treatments as was discussed above.

According to BÖHLER Edelstahl [45] structural materials for nuclear engineering purposes should exhibit a 0.2% proof stress of approximately 250 MPa at 100°C and 170 MPa at 400°C. The material used in that study from BÖHLER was a nickel-base alloy.

The Cu-Nb composite exhibits even at elevated temperatures around 300°C a hardness of approximately 1.2 GPa and hence an ultimate tensile strength of approximately 0.4 GPa or 400 MPa. The strength at 400°C should be in the range of 250 MPa.

According to the obtained results and the recommendation for structural materials for nuclear purposes from BÖHLER Edelstahl [45], this novel material offers excellent characteristics when considering hardness and strength. The maximum operating temperature of the Cu-Nb composite is below 400°C. The investigated composite could be used in pressurized water reactors and boiling water reactors [46], and produced in large scales for example via a process similar to friction stir welding [47].

5.3.2 Time dependent properties of the composite

The strain rate sensitivity (Fig. 4.27) from *Stage a*, as well as the activation volume of the flow stress (Fig. 4.28), were investigated in order to give more information of the plastic deformation behaviour. Although the governing deformation mechanism(s) at elevated temperature is a controversial issue in literature yet, a prediction for the investigated Cu-Nb composite will be attempted.

Strain rate sensitivity

As mentioned before, the SRS of a Cu-Nb composite has not been discussed in literature for the temperature region investigated in this work. The value should be in the range of approximately 0.020 at RT. This prediction arises from studies of fcc (Fig. 2.11 and Fig. 2.13) and bcc (Fig. 2.12) materials with a similar structure size, as well as comparative measurements by Dr. Maier. The SRS of the composite was determined to be in the range of 0.016.

The obtained SRS at RT for *Stage a* was approximately 0.019, which is in good accordance with the predicted values for similar materials with the same structure size, as well as the reference measurements by Dr. Maier. At this temperature it is expected that the plastic deformation is governed by a dislocation glide, where the dislocations interact with subgrains and grain boundaries for the fcc element Cu [39]. With increasing temperature the SRS for fcc elements should reach higher values, as was shown in (Fig. 2.13) and discussed in [32, 37, 39-41].

The rate limiting step for the bcc element Nb is the kink pair nucleation mechanism, because of the high Peierls stress at RT [25, 39] for bcc elements. At elevated temperatures (100°C and 200°C) the SRS exhibits no significant changes; the values stay nearly constant – indicating no significant change in the deformation behaviour. The first increase from approxi-

mately 0.020 to 0.055 is apparent at the testing temperature of 300°C. A similar behaviour was observed in previous investigations, for ufg Cu [35] and nc Ni [40], whereas nearly the same SRS values were observed.[4]

These results are in good agreement with the hardness measurements that were discussed in the previous chapter and shown in Fig. 4.20. The hardness as a function of temperature exhibits in the same temperature region a massive decrease of approximately 100%. This circumstance can be traced back to an increase of the SRS. Due to coarsening of at least one phase, where some grains coarsen but are still surrounded by an ufg matrix, thermally activated dislocation processes at grain boundaries can easily occur (thermally activated climb and annihilation of dislocation) [41]. The coarsening of at least one phase explains the loss of the hardness in this temperature region. The governing deformation mechanism – thermally activated interaction of dislocations with grain boundaries – does not change.

With increasing the temperature from 300°C to 400°C the SRS value rises again, from 0.055 to 0.110. The SRS of the novel Cu-Nb composite investigated in this work shows at this testing temperature the highest value. Further coarsening of the structure can explain these observations. With an increase in the amount of coarsened grains, dislocation climbing and annihilation is enhanced, resulting in a higher SRS value and a lower hardness. A bimodal microstructure of coarsened grains and ultrafine grains is expected to be apparent.

This increase is followed by a decrease of the SRS from 0.110 at 400°C to 0.060 at 500°C. This behaviour can be attributed to a coarsened microstructure (change from a bimodal distribution where some coarsened grains were embedded in an ufg matrix to a completely coarsened microstructure, as shown in Fig. 4.8) and was observed in prior studies [41] for Al shown in Fig. 2.15. At 500°C the thermal stability of the novel Cu-Nb composite is exceeded, due to the fact that the microstructure is no longer stable.

The ufg Al investigated by Göken et al. [41] exhibited the highest SRS value at a homologous temperature of 0.43; the novel composite investigated in this work showed the highest SRS at a homologous temperature of 0.50, when considering the melting point of Cu.

Moreover, the influence of impurities at grain boundaries on the SRS was discussed in [40]. It is proposed that a further rate limiting step is thermally activated depinning. Since Nb impurities at grain boundaries are expected to be in the Cu grains and vice versa, this mechanism

[4] Explanatory notes: Why does the composite behave like an fcc metal, although the second phase Nb is a bcc metal? The rate limiting process is contributed to screw dislocations (high Peierls stress) beneath the critical temperature. The bcc Nb *behaves like a fcc metal* due to the fact that the thermal contribution to flow stress is no longer apparent at testing temperatures above 135°C (= critical temperature for Nb) [39].

should also be mentioned. As described above, at 500°C the Nb can diffuse and hence no pinning should occur. This fact intensifies the specific trend of the SRS observed in this work.

Although the governing deformation mechanism for nc and ufg materials is controversially discussed, for example [3], it was assumed in this work that the plastic deformation is governed by a thermally activated dislocation interaction [39]. Grain boundary sliding or grain boundary rotation processes can be ruled out at elevated temperatures, since the microstructural dimensions are still in the range of 100 nm [41]. Moreover, diffusion processes can be excluded, because the observed SRS are far below values that are related to diffusion dominated deformation processes.

Activation volume

In order to verify these assumptions, the activation volume of the plastic flow was determined by two different methods, as was described in chapter 2.2. If no significant changes in the activation volume are observed, the governing deformation mechanism stays constant. The activation volume was calculated with the Burger's vector of a Cu-Nb composite [44] and shown in Fig. 4.28. For cg fcc materials high values in the order of 1000 b^3 are observed for a dislocation interaction (table 2.1) – the obstacle for glissile dislocations are forest dislocations and the cutting and interaction of these forest dislocations is the rate depending step, for example [35].

The Cu-Nb composite has a nominal grain size of approximately 100 nm and has an activation volume at RT of approximately 10 b^3. In accordance with Fig. 2.15 for fcc elements, the governing deformation mechanism for Cu is expected to be a dislocation interaction with subgrains and grain boundaries at RT. This was also proposed in [35, 39]. The activation volume for bcc elements, and hence for Nb, is assumed to be in the order of 10 b^3 for the nucleation of kink pairs below the critical temperature [40]. At 100°C the activation volume stays nearly constant, indicating no significant changes in the deformation mechanism and hence in the microstructure of the composite. The dislocation interaction with grain boundaries is still apparent, as well as the nucleation of kink pairs. Due to this the SRS exhibits no significant changes in this region. At 200°C and 300°C the activation volume doubles to prior values for both analysing methods. In this region (between 200°C and 300°C) the SRS value rises from a constant plateau up to 300°C. This could be an indication for a change in the microstructure – to a bimodal structure, as it was assumed in the discussion of the SRS and in [41].[5]

[5] Explanatory notes: In this temperature region the bcc element Nb behaves like an fcc metal and thus the deformation should not be affected by the nucleation of kink pairs.

Nonetheless, from RT to temperatures up to 300°C, the two analysing methods show good correlation of the results and nearly constant values for the activation volume. This behaviour indicates no significant changes in the deformation mechanism; plastic deformation is governed by thermally activated dislocation processes.

At higher temperatures (400°C and 500°C) the values of the activation volume are getting higher when considering the analysing method from equation 2.11. The activation volume of the second analysing method according to equation 2.12 does not change significantly. The difference between these two observed curves is related to thermal drift induced errors.

The first method is stronger influenced by drift errors, due to the fact that the hardness with a longer dwell time (and thus higher drift errors) is considered in the analysis. In the second method the hardness with the short dwell time of 5 seconds is used for the calculation. Thus, the introduced error does not affect the results in a significant way. According to the second method from Fig. 4.28 the activation volume as a function of temperature slightly increases from 10 b^3 to 42 b^3. The deformation mechanism is still a thermally activated dislocation interaction. This evaluation supports the analysis based on SRS changes.

5.3.3 Activation energy of plastic deformation

Finally, the activation energy of plastic deformation was calculated and compared to the activation energy of pure Cu. The data of the activation energy for pure Cu was obtained by an analysis from data shown in [33, 48] and equation 2.13. To obtain the activation energy for plastic deformation, a graphical analysis was carried out as shown below.

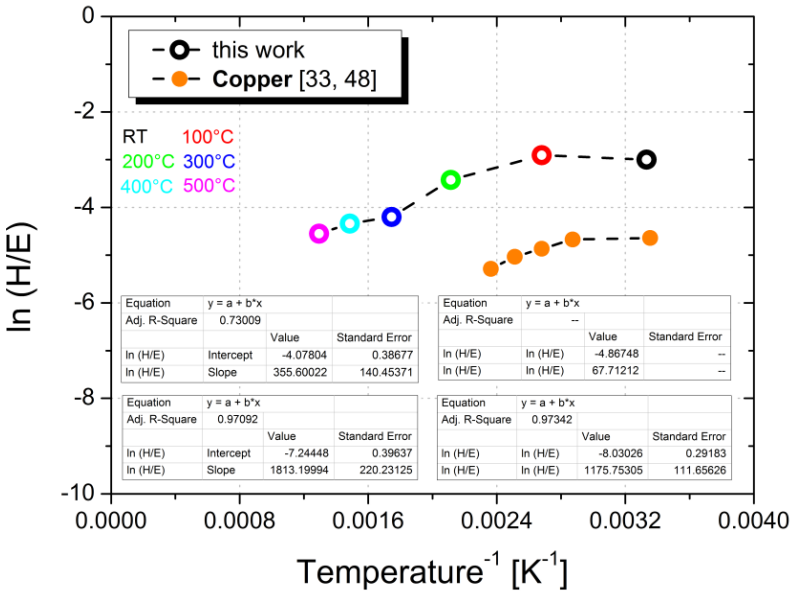

Fig. 5.6: Activation energy for plastic deformation for pure Cu [33, 48] and the Cu-Nb composite.

The activation energy for Cu from RT to 75°C shows a value of 0.6 kJ/mol and in the region from 75°C to 150°C a value of 10 kJ/mol, respectively. The calculated value for the Cu-Nb composite for the stage from RT to 200°C is approximately 3 kJ/mol. The stage from 200°C to the maximum testing temperature of 500°C gives a value of 15 kJ/mol.

According to [32] for ufg Al an activation energy for plastic deformation of ~ 7 kJ/mol can be related to *lattice controlled dislocation glide and is dependent on the Peierls stress*. Furthermore, an activation energy of ~ 15 kJ/mol is attributed to the *dislocation climb along grain boundaries,* and ~ 32 kJ/mol for cg materials (*dislocation intersection and cross slip*).

These findings confirm the observed values for the strain rate sensitivity and the activation volume. The plastic deformation is governed by dislocation climb along grain boundaries and annihilation of dislocations in the temperature range from 200°C to 400°C.

Compared to Cu, in the composite both regimes are moved to higher specific hardness values and higher temperatures. Therefore, the material is expected to have a better thermal stability than the mentioned pure Cu.

6 Summary

In general, composites are promising engineering materials for prospective purposes in various fields, ranging from applications in medicine to the energy technology [1, 2]. Furthermore, it is well known that a decrease of the structure size of a material to the nanocrystalline (nc) or ultrafine grained (ufg) range results for example in a higher hardness, or in better physical properties [2, 3]. It is evident that a composite material with a structure size in the nc or ufg regime should possess outstanding properties.

In previous investigations it was shown that nanoscaled body centred cubic (bcc) – face centred cubic (fcc) composites exhibit such outstanding properties in various fields. One of these materials is the composite assembled by the fcc element copper (Cu) and the bcc element niobium (Nb) [5-13]. Layered Cu-Nb composites have shown, for example, a high thermal stability [8, 9] as well as a high radiation damage tolerance [11-13], making them interesting for prospective use in nuclear reactors.

In this work, a high pressure torsion process [14-17], the *two step* high pressure torsion technique [17], was used to create a polycrystalline Cu-Nb composite in the ufg regime. The field of application for this material is at high temperatures in harsh radiation environments. The composite exhibits a microstructure in the range of approximately 100 to 200 nm. Several mechanical properties and the governing rate dependent deformation behaviour as a function of temperature were investigated using high temperature nanoindentation at elevated temperature up to 500°C. The hardness at room temperature with 5.4 GPa is significantly higher compared to other Cu-Nb composites. After long time testing at higher temperatures the material still exhibits a hardness of 3.0 GPa, whereas the ufg microstructure is stable up to 500°C. Furthermore, the governing deformation mechanisms are proposed to be dislocation glide in the fcc Cu [35-37, 39] and the nucleation of kink pairs in the bcc Nb [25, 39, 40] in the lower temperature region from room temperature up to 200°C, indicated by a strain rate sensitivity of $\sim$ 0.020 and an apparent activation volume of $\sim$ 10 b^3. With increasing temperature a change occurred to $\sim$ 0.110 and $\sim$ 25 b^3 respectively, whereas plastic deformation is governed by dislocation climb and annihilation at grain boundaries [41]. This hint is supported by temperature dependent changes in hardness and activation energy as determined from the high temperature nanoindentation experiments.

The outcomes of this work are a novel polycrystalline Cu-Nb composite with a high thermal stability. The mechanical properties and the governing deformation behaviour were determined. The investigated composite could be produced in large scales via a process similar to friction stir welding, making it interesting for nuclear purposes

7 Acknowledgements

First of all I would like to thank Assoc. Prof. Dr. Daniel Kiener, my supervisor, for offering me the opportunity to broaden my horizon by means of allowing me to do my master thesis at the Department of Materials Physics, Montanuniversität Leoben. I enjoyed the detailed and fruitful discussions about materials science in general, micromechanics issues and topics related to the deformation behaviour of materials. He has always been supportive and giving me encouraging and critical advice whenever I needed them.

I am very grateful to Ass. Prof. Dr. Peter Hosemann, for giving me the opportunity to perform an important part of my master thesis at the Department of Nuclear Engineering, University of California Berkeley. I will always remember his patience, enthusiasm and his deep understanding of materials. I would like to thank Dr. Marisa Rebelo de Figueiredo and Dr. Manuel David Abad, for the introduction to nanoindentation, the assistance during the high temperature experiments and specific discussion about different analysing methods.

My time at the UC Berkeley and in the Bay Area will be unforgettable thanks to the special colleagues and friends I met there. I would like to take this opportunity to thank some of them, especially my daily labmates – Cameron, David, Fritz and Scott, my football team *Goaldiggers*, as well as Sadegh. They made my stay in Berkeley remarkable and amazing.

I am thankful to my colleagues in Leoben, especially Dr. Verena Maier for scientific discussions about general aspects of high temperature nanoindentation, as well as the comparative measurements performed at the Friedrich-Alexander University, Erlangen-Nürnberg. Special thanks to Ruth and Christoph, for answering my questions and helping me whenever they could. We had a very specific but funny atmosphere in our office. Furthermore, I would like to express my thanks to Silke for advices during sample preparation, to Franz, for the preparation of the plungers, and Peter, for the suggestions related to high pressure torsion.

People, who I should not and will not forget, are my friends in Leoben – especially Jacoba, Chris and Michael, and the members of my football team *Team West* – especially David, Klaus, Oliver and Simon, as well as my companions – Felix, Paul, Stefan H. and Stefan R. We went together through all the ups and downs of undergraduate studies. Thanks to the nice discussions, when preparing for exams, and the time we spent together. Furthermore, I am grateful to Marius, with whom I shared a long life time starting from high school, the materials science studies in Leoben and the research stay in Berkeley. We were pushing each other to achieve the highest possible results.

I would also specially like to thank a unique person of my life – Maria. She has always been there for me, cheered me up, and listened to my explanations about how interesting or exhausting my days in Leoben were. Thanks a lot for that.

Finally, I would like to thank my family for their support and encouragement. My parents, Zorica and Milenko, as well as my sisters, Adriana and Ana-Maria, and my brother, Antun. They helped me to achieve this goal I set myself some time ago. I want to thank them for their patience, understanding, and happiness during the last years.

Last but not least, I am grateful to the Austrian Marshall Plan Foundation, the Montanuniversität Leoben, and the province of Lower Austria, for research grants concerning the stay at the UC Berkeley. Special thanks to Dr. Cornelius Grupp for financial supporting during my whole time at the Montanuniversität Leoben. Without these scholarships it would have been impossible to accomplish my work and the studies in this way.

8 Abbreviations

AF	area function
AV	activation volume
bcc	body centered cubic
BSD	back scatter detector
cBN	cubic boron nitride
cg	coarse grained
CL	constant load
CRL	constant rate of loading
CSM	constant stiffness method
CSR	constant strain rate
Eq.	equation
e.g.	exempli gratia
FAU	Friedrich-Alexander University
fcc	face centered cubic
Fig.	figure
HPT	high pressure torsion
i.e.	id est
LM	light microscope
nc	nanocrystalline
RT	room temperature
SEM	scanning electron microscope
SPD	severe plastic deformation
SRS	strain rate sensitivity
ufg	ultrafine grained

9 References

[1] H. Gleiter, “Nanocrystalline Materials”, *Progress in Materials Science 33,* pp. 223-315, 1989.

[2] Y. Zhu, et al., “Performance and applications of nanostructured materials produced by sever plastic deformation”, *Scripta Materialia 51,* pp. 825-830, 2004.

[3] M. Meyers, et al., “Mechanical properties of nanocrystalline materials”, *Progress in Materials Science 51,* pp. 427-556, 2006.

[4] “Chemsoc periodic table”, 2013. [Online]. Available: http://chemsoc.velp.info/alloys/Cu-Nb.jpg. [Accessed November 2013].

[5] E. Botcharova, et al., “Supersaturated solid solution of niobium in copper by mechanical alloying”, *Journal of Alloys and Compounds 351,* pp. 119-125, 2003.

[6] E. Botcharova, et al., “Mechanical alloying of copper with niobium and molybdenum”, *Journal of Materials Science 39,* pp. 5287-5290, 2004.

[7] E. Botcharova, et al., “High thermal stability of mechanically-alloyed nanocrystalline Cu-Nb alloys”, *International Journal of Materials Research 97,* pp. 1350-1354, 2006.

[8] A. Misra, et al., “Effects of elevated temperature annealing on the structure and hardness of copper/niobium nanolayered films”, *Journal of Materials Research 20,* pp. 2046-2054, 2005.

[9] N. Mara, et al., “High-temperature mechanical behavior/microstructure correlation of Cu/Nb nanoscale multilayers”, *Materials Science and Engineering A 493,* pp. 274-282, 2008.

[10] N. Mara, et al., “Tensile behavior of 40 nm Cu/Nb nanoscale multilayers”, *Scripta Materialia 58,* pp. 874-877, 2008.

[11] A. Misra, et al., “The Radiation Damage Tolerance of Ultra-High Strength Nanolayered Composites”, *JOM,* pp. 62-65, 2007.

[12] X. Zhang, et al., “Nanostructured Cu/Nb multilayers subjected to helium ion-irradiation”, *Nuclear Instruments and Methods in Physics Research Section B: Beam Interactions with Materials and Atoms 261,* pp. 1129-1132, 2007.

[13] N. Li, et al., “Defect structures and hardening mechanism in high dose helium ion implanted Cu and Cu/Nb multilayer thin films”, *International Journal of Plasticity 32-33,* pp. 1-16, 2012.

[14] R. Pippan, et al., “Saturation of Fragmentation During Severe Plastic Deformation”, *Annual Review of Materials Research 40,* pp. 19-43, 2010.

[15] A. Vorhauer, et al., “On the homogeneity of deformation by high pressure torsion”, *Scripta Materialia 51,* pp. 921-925, 2004.

[16] I. Sabirov, et al., “Fabrication of a W-25%Cu nanocomposite by high pressure torsion”, *Materials Science Forum,* pp. 561-566, 2006.

[17] A. Bachmeier, et al., “The formation of supersaturated solid solutions in Fe-Cu alloys deformed by high-pressure torsion”, *Acta Materialia 60,* pp. 860-871, 2012.

[18] A. C. Fischer-Cripps, Introduction to Contact Mechanics, New South Wales: Springer, 2007.

[19] V. Maier, “PhD thesis, Friedrich-Alexander University, Erlangen-Nurnberg”, 2013.

[20] C. Schuh, et al., “New regime of homogenous flow in the deformation map of metallic glasses: elevated temperature nanoindentation experiments and mechanistic modeling”, *Acta Materialia 52,* pp. 5879-5891, 2004.

[21] B. Beake, et al., “Nanoscale materials testing under industrially relevant conditions: high-temperature nanoindentation testing”, *International Journal of Materials Research 94,* pp. 798-801, 2003.

[22] B. Beake, et al., “High-temperature nanoindentation testing of fused silica and other materials”, *Philosophical Magazine A 82,* pp. 2179-2186, 2002.

[23] N. Everitt, et al., “High temperature nanoindentation - the importance of isothermal contact”, *Philosophical Magazine 91,* pp. 1221-1244, 2011.

[24] M. Mayo, et al., “A micro-indentation study of superplasticity in Pb, Sn, and Sn-38 wt% Pb”, *Acta Metallurgica 36,* pp. 2183-2192, 1988.

[25] J. Alkorta, et al., “Critical examination of strain-rate sensitivity measurement by nanoindentation methods: Application to severely deformed niobium”, *Acta Materialia 56,* pp. 884-893, 2008.

[26] V. Maier, et al., “Nanoindentation strain-rate jump tests for determining the local strain-rate sensitivity in nanocrystalline Ni and ultrafinegrained Al”, *Journal of Materials Research 26,* pp. 1421-1430, 2011.

[27] B. Lucas, “PhD Thesis, University of Tennessee, Knoxville”, 1997.

[28] B. Lucas, et al., “Indentation Power-Law Creep of High-Purity Indium”, *Metallurgical and Materials Transaction A 30,* p. 601, 1999.

[29] M. Mayo, et al., “Mechanical Properties of Nanophase TiO2 as Determined by Nanoindentation”, *Journal of Materials Research 5,* pp. 1073-1082, 1990.

[30] M. Mayo, et al., “Nanoindentation of Nanocrystalline ZnO”, *Journal of Materials Research 7,* pp. 973-979, 1992.

[31] D. Peykov, et al., “Evaluation of strain rate sensitivity by constant load nanoindentation”, *Journal of Materials Science 47,* pp. 7189-7200, 2012.

[32] J. Wheeler, et al., “Activation parameters for deformation of ultrafine-grained aluminium as determined by indentation strain rate jumps at elevated temperatures”, *Materials Science & Engineering A 585,* pp. 108-113, 2013.

[33] G. Simmons, et al., “Single Crystal Elastic Constants and Calculated Aggregate Properties”, Cambridge, Massachusetts, and London, England, The MIT Press, pp. 178-233.

[34] A. Argon, Strengthening Mechanisms in Crystal Plasticity, Oxford: Oxford Materials, 2008.

[35] J. Chen, et al., “Hardness and strain rate sensitivity of nanocrystalline Cu”, *Scripta Materialia 54,* pp. 1913-1918, 2006.

[36] B. Farrokh, et al., “Grain size, strain rate, and temperature dependence of flow stress in ultra-fine grained and nanocrystalline Cu and Al: Synthesis, experiment, and constitutive modeling”, *International Journal of Plasticity 25,* pp. 715-732, 2009.

[37] S. Tao, et al., “Experimental investigation on strain rate sensitivity of ultra-fine grained copper at elevated temperatures”, *Mechanics of Materials 43,* pp. 111-118, 2011.

[38] R. Carreker, et al., “Tensile deformation of high-purity copper as a function of temperature, strain rate, and grain size”, *Acta Metallurgica 1,* pp. 654-663, 1953.

[39] Q. Wei, et al., “Effect of nanocrystalline and ultrafine grain sizes on the strain rate sensitivity and activation volume: fcc versus bcc metals”, *Materials Science and Engineering A 381,* pp. 71-79, 2004.

[40] Y. Wang, et al., “Temperature-dependent strain rate sensitivity and activation volume of nanocrystalline Ni”, *Acta Materialia 54,* pp. 2715-2726, 2006.

[41] M. Göken, et al., “Grain Refinement and Deformation Mechanisms in Heterogeneous Ultrafine-Grained Materials Processed by Accumulative Roll Bonding”, *Proceedings 33rd Risø Symposium On Materials Science: Nanometals – Status and Perspective*, pp. 31-48, 2012.

[42] X. Sauvage, et al., “Nanostructure and properties of a Cu-Cr composite processed by severe plastic deformation”, *Scripta Materialia 58,* pp. 1125-1128, 2008.

[43] “WebElements periodic table”, 2013. [Online]. Available: http://www.webelements.com/. [Accessed November 2013].

[44] X. Zhu, et al., “Microstructure and ultrahigh strength of nanoscale Cu/Nb multilayers”, *Thin Solid Films 520,* pp. 818-823, 2011.

[45] “Boehler Edelstahl”, 2013. [Online]. Available: http://www.bohler-edelstahl.com/files/L276DE.pdf. [Accessed November 2013].

[46] S. Zinkle, et al., “Materials challenges in nuclear energy”, *Acta Materialia 61,* pp. 735-758, 2013.

[47] R. Mishra, et al., “Friction stir processing: a novel technique for fabrication of surface composite”, *Materials Science and Engineering: A 341,* pp. 307-310, 2003.

[48] J. Bach, et al., “Influence of grain boundaries on the deformation resistance: Insight from an investigation of deformation kinetics and microstructure of copper after predefromation by ECAP” *Philosophical Magazine 93,* pp. 4331-4354, 2013.